THE JOURNAL OF PHYSICAL CHEMISTRY A

Subscriber access provided by Universitätsbibliothek Bern

Article

Excitonic Splitting and Vibronic Coupling Analysis of the *Meta*-Cyanophenol Dimer

Franziska A Balmer, Sabine Kopec, Horst Koeppel, and Samuel Leutwyler

J. Phys. Chem. A, **Just Accepted Manuscript** • DOI: 10.1021/acs.jpca.6b10416 • Publication Date (Web): 06 Dec 2016

Excitonic Splitting and Vibronic Coupling Analysis of the meta-Cyanophenol Dimer

Franziska A. Balmer,[†] Sabine Kopec,[‡] Horst Köppel,[‡] and Samuel Leutwyler[*,†]

Department of Chemistry and Biochemistry, University of Bern, Freiestrasse 3, CH-3012 Bern, Switzerland, and Theoretische Chemie, Physikalisch-Chemisches Institut, Universität Heidelberg, Im Neuenheimer Feld 229, D-69120 Heidelberg, Germany.

E-mail: leutwyler@dcb.unibe.ch

Abstract

The S_1/S_2 splitting of the *meta*-cyanophenol dimer, $(mCP)_2$, and the delocalization of its excitonically coupled S_1/S_2 states are investigated by mass-selective two-color resonant two-photon ionization and dispersed fluorescence spectroscopy, complemented by a theoretical vibronic coupling analysis based on correlated *ab initio* calculations at the approximate coupled cluster CC2 and SCS-CC2 levels. The calculations predict three close-lying ground-state minima of $(mCP)_2$: The lowest is slightly Z-shaped (C_i-symmetric), the second-lowest is < 5 cm^{-1} higher and planar (C_{2h}). The vibrational ground state is probably delocalized over both minima. The $S_0 \rightarrow S_1$ transition of $(mCP)_2$ is electric-dipole allowed ($A_g \rightarrow A_u$), while the $S_0 \rightarrow S_2$ transition is forbidden ($A_g \rightarrow A_g$). Breaking the inversion symmetry by ^{12}C/^{13}C- or H/D-substitution renders the $S_0 \rightarrow S_2$ transition partially allowed; the excitonic contribution to the S_1/S_2 splitting is $\Delta_{exc} = 7.3$ cm^{-1}. Additional isotope-dependent contributions arise from

[*]To whom correspondence should be addressed

[†]Department of Chemistry and Biochemistry, University of Bern, Freiestrasse 3, CH-3012 Bern, Switzerland

[‡]Theoretische Chemie, Physikalisch-Chemisches Institut, Universität Heidelberg, Im Neuenheimer Feld 229, D-69120 Heidelberg, Germany.

the changes of the *m*-cyanophenol zero-point vibrational energy upon electronic excitation, which are $\Delta_{iso}(^{12}C/^{13}C) = 3.3$ cm^{-1} and $\Delta_{iso}(H/D) = 6.8$ cm^{-1}. Only partial localization of the exciton occurs in the $^{12}C/^{13}C$ and H/D substituted heterodimers. The SCS-CC2 calculated excitonic splitting is $\Delta_{el} = 179$ cm^{-1}; when multiplying this with the vibronic quenching factor $\Gamma^{exp}_{vibron} = 0.043$, we obtain an exciton splitting $\Delta^{exp}_{vibron} = 7.7$ cm^{-1}, which agrees very well with the experimental $\Delta_{exc} = 7.3$ cm^{-1}. The semiclassical exciton hopping times range from 3.2 ps in $(mCP)_2$ to 5.7 ps in the heterodimer (mCP-*h*)·(mCP-*d*). A multimode vibronic coupling analysis is performed encompassing all the vibronic levels of the coupled S_1/S_2 states from the v=0 level to 600 cm^{-1} above. Both linear and quadratic vibronic coupling schemes were investigated to simulate the $S_0 \rightarrow S_1/S_2$ vibronic spectra, those calculated with the latter scheme agree better with experiment.

1 Introduction

Excitonic interactions between chromophores play an important role for electronic energy transfer in a wide range of photochemical and biological systems such as conjugated polymers, molecular crystals and photosynthetic light-harvesting complexes.[1–8] Gas-phase hydrogen-bonded molecular dimers can be used to investigate these interactions since they are representative of larger systems, but are still small enough to yield well-resolved vibronic spectra and allow high-level *ab initio* calculations and vibronic coupling treatments. We have been studying the excitonic $S_0 \rightarrow S_1/S_2$ splittings in rigid, doubly H-bonded aromatic dimers such as $(2\text{-pyridone})_2$, $(2\text{-aminopyridine})_2$, $(\text{benzoic acid})_2$, $(\text{benzonitrile})_2$ and $(\textit{ortho}\text{-cyanophenol})_2$ by mass- and isotope-selective two-color resonant two-photon ionization (2C-R2PI) spectroscopy with vibronic coupling calculations.[9–18] These dimers are all inversion-symmetric, which implies that the S_1 excited states of their constituent monomers *A* and *B* are degenerate at large intermolecular distance. When the doubly H-bonded dimer is formed, the intermolecular coupling splits the monomer states into two nondegenerate excitonic states, one of which is symmetric (*g*) and the other antisymmetric (*u*), rendering the $S_0 \rightarrow S_1/S_2$ electronic transitions forbidden and allowed, respectively. Isotopic substitution

breaks the inversion symmetry of the dimer sufficiently to render the forbidden excitonic transition allowed, enabling to experimentally determine the $S_1 \leftrightarrow S_2$ excitonic splitting.[9–18]

We have previously shown that the coupling of the S_1 and S_2 states to excited-state intra- and intermolecular vibrations has a substantial impact on the magnitude of the excitonic energy splittings.[13,16] The observed splittings are up to 40 times smaller than the electronic Davydov splittings that are predicted by *ab initio* calculations.[9–18] This so-called "vibronic quenching" of the electronic excitonic splitting can be explained by taking the vibrational normal modes into account within Förster's perturbation theory approach[19] and the Fulton-Gouterman model.[20,21] Applying the vibronic quenching factor Γ_{vibron} to the calculated Davydov splitting resulted in vibronic splittings very close to the experimentally observed S_1/S_2 splittings.[13,15,17]

Here, we combine experimental spectroscopic investigations, *ab initio* calculations and vibronic-coupling theory treatments to explain the S_1/S_2 state excitonic splitting and vibronic band structure of the *meta*-cyanophenol dimer, $(mCP)_2$. In contrast to the previously studied doubly H-bonded dimers,[9–18] the $S_0 \rightarrow S_1$ transition of $(mCP)_2$ is fully allowed, while the $S_0 \rightarrow S_2$ transition is forbidden. This is due to the orientation of the mCP monomer electronic transition dipole moments, relative to the inter-monomer vector R_{AB} between the centers of mass of A and B, see Figure 1.

Zehnacker and co-workers have previously studied mCP and $(mCP)_2$ by laser-induced fluorescence and fluorescence dip-IR spectroscopy.[22] They observed both the cis- and trans-mCP rotamers, whose OH groups are oriented towards and away from the CN group. They reported that the *meta*-cyanophenol dimer, $(mCP)_2$, is dominantly formed by the cis-mCP rotamer, which can form two antiparallel OH$\cdots$N hydrogen bonds, while the trans-mCP dimer, which can only form a single H-bond, was not observed experimentally.[22] They proposed vibronic assignments of the observed bands and identified several fundamental transitions of non-totally-symmetric vibrations. In C_i-symmetry, these transitions would not be allowed. Hence, Zehnacker and co-workers concluded a loss of symmetry upon excitation that renders the fundamental transitions of non-totally symmetric vibrations allowed; the loss of symmetry was thought to cause a localization of the electronic excitation on one of the monomers.[22]

Below, we present the mass-selected two-color resonant two-photon ionization spectra of the homodimers $(mCP)_2$ and $(mCP\text{-}d)_2$, and of the singly isotopically substituted (mCP)·(mCP-^{13}C) and (mCP-*h*)·(mCP-*d*) heterodimers. From the latter two spectra we determine the S_1/S_2 splittings and the contribution of the ^{12}C/^{13}C and H/D isotopic mass changes on the splitting, similar to $(\text{benzoic acid})_2$ and $(\text{benzonitrile})_2$.[14,15] A computational investigation of the $(mCP)_2$ ground state using correlated *ab initio* methods reveals four different minimum-energy structures. The normal modes of the two lowest-energy structures form the basis for the following vibronic coupling treatment and band assignments in the spectrum of $(mCP)_2$. The linear and quadratic vibronic coupling schemes are employed[23] to simulate the theoretical vibronic spectra. The influence of the vibronic coupling on the excitonic energy splitting is discussed and the question of the localization of the excited states addressed. While the S_1/S_2 coupled states are completely delocalized in the $(mCP)_2$ and $(mCP\text{-}d)_2$ homodimers, asymmetric isotopic substitution partially localizes the two electronic transitions. Using the effective-mode approximation introduced by Köppel and co-workers,[24] we show that the double-minimum character of the lower excited state of the homodimer does *not* imply a localization of the excitation as proposed by Zehnacker and co-workers.[22]

2 Theoretical Framework for Multimode Vibronic Coupling

Recently, Köppel and co-workers have extended the analysis from the S_1/S_2 splitting to simulating the six-dimensional vibronically coupled spectra of $(o\text{-cyanophenol})_2$ and $(2\text{-pyridone})_2$, and compared them to the 2C-R2PI spectra.[16,18] The representation of the vibronic coupling in the framework of the Fulton-Gouterman model[20,21] was seen to be insufficient. Instead they adopted the more general linear and quadratic vibronic coupling schemes.[16,18,23] These naturally include certain important intermolecular normal modes in the analysis, resulting in convincing simulations of the $S_0 \rightarrow S_1/S_2$ vibronic spectra that were in good agreement with experiment.[16,18] Other extensions of the Fulton-Gouterman model to vibronic coupling in excitonic systems have been made, see, for example, the application to bichromophores by Slipchenko, Zwier and co-workers.[25–27]

2.1 The Multimode Vibronic Coupling Model

The $S_0 \rightarrow S_1/S_2$ vibronic spectrum of $(mCP)_2$ is investigated by means of the multimode vibronic coupling model described in ref. 23, including 12 vibrational modes, of which seven are totally-symmetric (a_g) and five are non-totally symmetric (a_u). This model has been applied before to (*ortho*-cyanophenol)$_2$ and (2-pyridone)$_2$, and is there explained in detail.[16,18] The Hamiltonian is constructed in a diabatic basis with a diagonal nuclear kinetic energy operator T_N and a coupling matrix $\mathbf{W}$ emerging from the potential energy part.

$$H = T_N \mathbf{1} + \mathbf{W}(\mathbf{Q}) \tag{1}$$

The coupling matrix elements are smooth functions of the dimensionless normal mode coordinates Q_i, and are expanded in a Taylor series around the ground-state equilibrium geometry $Q_0 = 0$. To obtain the linear (LVC) and quadratic (QVC) vibronic coupling models, the Taylor-series is truncated after the first and second order term, respectively.[18,23]

Coupling constants are the building blocks of the coupling matrix and are restricted by symmetry selection rules, determining which vibrational normal modes are relevant in the diagonal and off-diagonal elements. Vibrational modes with irreducible representation Γ_Q can couple electronic states 1 and 2 with corresponding irreducible representations Γ_1 and Γ_2 only if their direct product comprises the totally symmetric representation Γ_{A_g}.

$$\Gamma_1 \otimes \Gamma_Q \otimes \Gamma_2 \supset \Gamma_{A_g}. \tag{2}$$

In the linear vibronic coupling model, the totally symmetric normal modes (index g) lead to *intrastate* coupling, while non-totally symmetric normal modes (index u) lead to *interstate* coupling, if their symmetry is compatible with Equation 2 (in the point group of interest). $(mCP)_2$ is C_i-symmetric (see below), hence, only a_g and a_u vibrations exist. The symmetries of the two excited electronic states of interest are A_g and A_u, thus all modes are relevant for the coupling matrix. A

double-well structure of the lower electronic state along the respective normal mode coordinate Q_u arises if the interstate coupling constants are sufficiently large. The totally symmetric modes (tuning modes) affect the energy separation between the coupled electronic states.[23] The multimode *linear* vibronic coupling Hamiltonian comprising two electronic states is defined as:[23]

$$\mathbf{W}^{(1)}(\mathbf{Q_g},\mathbf{Q_u}) = \sum_{i,j} V_0(Q_{gi},Q_{uj})\mathbf{1} + \begin{pmatrix} E_1 + \sum_i \kappa_i^{(1)} Q_{gi} & \sum_j \lambda_j Q_{uj} \\ \sum_j \lambda_j Q_{uj} & E_2 + \sum_i \kappa_i^{(2)} Q_{gi} \end{pmatrix}, \tag{3}$$

where the ground state potential is given as $V_0(Q_{gi},Q_{uj}) = \frac{\hbar\omega_{gi}}{2}Q_{gi}^2 + \frac{\hbar\omega_{uj}}{2}Q_{uj}^2$. $E_{1,2}$ are the electronic excitation energies of the respective state, κ is the intrastate vibronic coupling constant and λ the interstate vibronic coupling constant. To include quadratic coupling terms, the Hamiltonian is extended. For reasons of simplicity, it is shown for a two-state/two-mode system including one tuning mode Q_g and one coupling mode Q_u:

$$\begin{aligned}\mathbf{W}^{(2)}(Q_g,Q_u) =& V_0(Q_g,Q_u)\mathbf{1} + \\ & \begin{pmatrix} E_1 + \kappa^{(1)}Q_g + \frac{1}{2}\gamma_g^{(1)}Q_g^2 + \frac{1}{2}\gamma_u^{(1)}Q_u^2 & \lambda Q_u + \frac{1}{2}\mu_{gu}Q_gQ_u \\ \lambda Q_u + \frac{1}{2}\mu_{gu}Q_gQ_u & E_2 + \kappa^{(2)}Q_g + \frac{1}{2}\gamma_g^{(2)}Q_g^2 + \frac{1}{2}\gamma_u^{(2)}Q_u^2 \end{pmatrix}\end{aligned} \tag{4}$$

The quadratic coupling constant γ accounts for frequency changes upon excitation. The mixed quadratic coupling μ_{gu} needs to be considered when analyzing multidimensional cuts through the potential energy surfaces (PESs). Here, we are only considering one-dimensional cuts and μ_{gu} is put to zero. Quite generally, all 2nd-order coupling terms off-diagonal in the vibrational modes ("Dushinsky mixing") are suppressed in the Hamiltonian. This is motivated by ample positive experience with the LVC model Hamiltonian which is already extended by the present approach (namely, including diagonal second-order coupling terms).

The adiabatic PES along the normal mode coordinates Q_g and Q_u are obtained by diagonaliza-

tion of the diabatic coupling matrix **W** and result in the following expressions:[23]

$$V_{1,2}(Q_g) = \frac{\hbar\omega_g}{2}Q_g^2 + \frac{\gamma_g^{(1,2)}}{2}Q_g^2 + \kappa^{(1,2)}Q_g + E_{1,2} \quad (5)$$

$$V_{1,2}(Q_u) = \frac{\hbar\omega_u}{2}Q_u^2 + \frac{E_1+E_2}{2} + \frac{\gamma_u^{(1)}+\gamma_u^{(2)}}{4}Q_u^2 \pm \sqrt{\left(\frac{E_2-E_1}{2} + \frac{\gamma_u^{(2)}-\gamma_u^{(1)}}{4}Q_u^2\right)^2 + (\lambda Q_u)^2} \quad (6)$$

From these PESs, the intrastate coupling constant κ and the quadratic coupling constant γ can be derived as follows:

$$\kappa^{(i)} = \frac{\partial V_i(Q)}{\partial Q_g}|_{Q=0} \quad (i=1,2) \qquad \gamma_g^{(i)} = \frac{\partial^2 V_i(Q)}{\partial Q_g^2}|_{Q=0} \quad (i=1,2; \text{for } \omega_g = 0) \quad (7)$$

The interstate coupling constant λ and the corresponding quadratic coupling constants γ_u are obtained from the sum and difference of the adiabatic PES, see below.

2.2 Dynamical Calculations

The $S_0 \rightarrow S_1/S_2$ vibronic spectra are simulated via wave-packet propagation with the multiconfigurational time-dependent Hartree (MCTDH) method.[28–30] The spectral intensity distribution $P(E)$ is obtained by Fourier transformation of the autocorrelation function $C(t)$.[29]

$$P(E) \propto \int e^{iEt}C(t)dt, \quad \text{with } C(t) = \langle\Psi(0)|\Psi(t)\rangle \quad (8)$$

$C(t)$ is a measure for the probability that the wave function at a time t is equal to the initial wave function. MCTDH uses a multiconfigurational wave function, which is the weighted sum over Hartree products of optimized time-dependent basis functions ϕ, called single-particle functions,

for every degree of freedom f.

$$\Psi(Q_1,...,Q_f,t) = \sum_{j_1=1}^{n_1} \cdots \sum_{j_f=1}^{n_f} A_{j_1 \cdots j_f}(t) \phi_{j_1}^{(1)}(Q_1,t) \cdots \phi_{j_f}^{(f)}(Q_f,t) \tag{9}$$

Equations of motion for the expansion coefficients A_j and the single-particle functions are derived through the Dirac-Frenkel variational principle.

3 Methods

3.1 Computational Methods

The mCP dimer was optimized with the approximate coupled-cluster singles and doubles method (CC2), using the resolution-of-identity (RI) and its spin-component scaled variant (SCS-CC2),[31–33] and the aug-cc-pVDZ and aug-cc-pVTZ basis sets. Four minimum-energy structures were found, which are discussed below. Vertical excitation energies to the S_1 and S_2 state were calculated at the minima using the SCS-CC2 method. The spin-component-scaled variant of the CC2 method was applied because it has recently been found to yield highly reliable results for the valence excitations of aromatic molecules.[34]

To calculate the vibronic lines in the $S_0 \rightarrow S_1/S_2$ spectrum, the $(mCP)_2$ ground state was optimized at the SCS-CC2/aVTZ level and normal-mode calculations were performed on this structure. One-dimensional cuts through the PESs were obtained by calculating the vertical SCS-CC2/aVTZ excitation energies at geometries that were displaced by $Q = \pm 0.5, \pm 1, \pm 2, \pm 3$ along the S_0 state normal-mode eigenvectors. All calculations were carried out using the Turbomole V6.3 program package.[35,36] For the mCP monomer, the PES needed to determine the Huang-Rhys factors to evaluate the quenching factor Γ were calculated in the same manner as for the dimer, but with the SCS-CC2/cc-pVTZ method.

3.2 Experimental Setup

The mCP dimers are produced in a pulsed supersonic expansion of mCP (Aldrich, 99%) heated to 80 °C, seeded in Ne carrier gas at $p_0 = 1.2$ bar and expanded through a 20 Hz repetition rate pulsed nozzle (0.4 mm diameter). Mass-selective two-color resonant two-photon ionization (2C-R2PI) spectra were recorded by crossing the skimmed molecular beam with temporarily and spatially overlapping excitation and ionization laser beams in the source chamber of a time-of-flight mass spectrometer. For excitation, the frequency doubled output of a Nd:YAG-pumped Radiant Dyes NarrowScan dye laser (Sulforhodamine B in EtOH) with a bandwidth of 0.04 cm^{-1} was used. All spectra were vacuum-corrected. For the ionization step we used an Ekspla NT342B UV optical parametric oscillator/optical parametric amplifier (OPO/OPA) operated at 245 nm (1 mJ/pulse).

The fluorescence emission spectra were measured by crossing the unskimmed molecular beam with the UV excitation laser beam, fixed at the mCP 0_0^0 band, about 4 mm downstream of the nozzle. The fluorescence emission was collected using a spherical mirror and quartz optics, dispersed in a SOPRA UHRS 1.5 m monochromator in second order and detected by a Peltier-cooled Hamamatsu R928 photomultiplier.

The ^{13}C-isotopomer spectra were measured using the natural ^{13}C abundance of 15.5% for $(mCP)_2$. Deuterated mCP was obtained by dissolving mCP in CD_3OD (99.8 atom-% D), refluxing for 3 hours, and evaporating the perdeuteromethanol, leading to ∼75% deuteration of the hydroxy group. The spectra of (mCP-*h*)(mCP-*d*) were recorded using mixtures of mCP-*h* and mCP-*d*.

4 Results

4.1 Equilibrium Geometries and Vibrational Analysis

Figure 2 shows the three lowest-energy $(mCP)_2$ structures, as optimized at the SCS-CC2/aug-cc-pVTZ level. The CC2 and SCS-CC2 calculated relative energies are listed in Table 1. A π-stacked geometry was found at the CC2 and SCS-CC2/aug-cc-pVDZ levels, but is predicted to

lie $270-470$ cm^{-1} higher; its structure is shown in Figure S1 (Supporting Information). The Cartesian coordinates of the four structures in Table 1 are given in Tables S1 to S4.

While both CC2 and SCS-CC2 predict that the Z-shaped C_i-symmetric and the C_{2h}-symmetric planar structure are degenerate when using the aug-cc-pVDZ basis set, the SCS-CC2/aug-cc-pVTZ calculation yields minima differing by 0.1 cm^{-1}. With CC2/aVTZ the C_{2h} structure is an index-1 saddle point 5.5 cm^{-1} above the C_i global minimum. All calculations predict a third "V-shaped" and C_2-symmetric structure $3-11$ cm^{-1} above the global minimum. Zehnacker and co-workers optimized $(mCP)_2$ at the B3LYP/6-31G** level, which also yielded a C_i-symmetric structure.[22]

In C_i symmetry all calculations predict the planes of the mCP subunits to be displaced along the z-axis, see Figure 2. The calculated displacement distance is $\Delta z = \pm 0.12$ Å with CC2 and ± 0.03 Å with SCS-CC2, using the aug-cc-pVTZ basis set. Figure 2 also shows the low-frequency large-amplitude intermolecular vibrations that interconvert these structures. The C_{2h} and two symmetry-equivalent C_i minima are connected by the "stagger" vibration δ. The V-shaped C_2 structure is interconverted to its enantiomer via the planar C_{2h} structure by the β "bending" vibration. Given the tiny energy differences between the C_{2h} and C_i minima, the barrier along the δ vibrational coordinate is probably so small that the lowest vibrational level is delocalized over all three minima. Below, we will consider the SCS-CC2/aVTZ results only.

4.2 $S_0 \rightarrow S_1/S_2$ Electronic Transitions

An important difference between $(mCP)_2$ and the previously investigated H-bonded dimers[9–18] is that in $(mCP)_2$ the $S_0 \rightarrow S_1$ transition is $^1A_g \rightarrow ^1B_u$ and electric-dipole allowed, while the $S_0 \rightarrow S_2$ transition is $^1A_g \rightarrow ^1A_g$ and dipole-forbidden. In the previously investigated dimers, the angle between the transition dipole moments (TDM) of the monomer moieties and the intermonomer vector R_{AB} is larger than the "magic angle" $\theta_m = 54.7°$ for dipole↔dipole interactions, which is given by $cos^2(\theta_m) = 1/3$. The calculated TDM angles are $\theta = 85°$ in $(2\text{-pyridone})_2$,[13] 88° in $(\text{benzoic acid})_2$,[13] 59° in $(ortho\text{-cyanophenol})_2$,[17] 77° in $(2\text{-aminopyridine})_2$,[17] and 63° in $(\text{benzonitrile})_2$.[15] For $(mCP)_2$ however, both the CC2 and SCS-CC2 calculations predict that $\theta = 11°$, i.e., that the

TDMs are nearly collinear, as shown in Figure 1.

The relative intensities of the $S_0 \rightarrow S_1$ and $S_0 \rightarrow S_2$ transitions depend on the θ, as schematically depicted in Figure 3(a,b). As θ decreases, the TDM orientation changes from parallel/antiparallel, Figure 3(a), to collinear/anti-collinear in Figure 3(b). As shown to the left of Figure 3(a,b), the transition-dipole $\leftrightarrow$ transition-dipole interaction splits the S_1 and S_2 states by the energy V_{dd}:

$$V_{dd} = \frac{|\vec{\mu}_A||\vec{\mu}_B|}{4\pi\varepsilon_0 R_{AB}^3} \cdot \left(2cos^2\theta + sin^2\theta \cdot cos\phi\right) \tag{10}$$

where ϕ is zero if the two molecules are coplanar.

The calculated vertical excitation energies are given in Table 2. All calculations agree that the $S_0 \rightarrow S_2$ transition is forbidden in C_i and C_{2h} symmetries, while it is weakly allowed in C_2. The CC2 and SCS-CC2 calculated vertical excitation energies of the C_i, C_{2h} and C_2 isomers change only by a few cm^{-1} between different method/basis set combination, see Table 2, and the purely electronic S_1/S_2 splittings are between 173 and 201 cm^{-1}.

4.3 Dispersed Fluorescence Spectrum

The dispersed fluorescence (DF) spectrum of $(mCP)_2$ was measured by exciting at the $S_0 \rightarrow S_1$ 0_0^0 band (33255 cm^{-1}) and is shown in Figure 4. Overall, the DF spectrum agrees well with that of Zehnacker and co-workers and many vibrational assignments are the same as those proposed in reference 22. However, we have changed the assignments of the δ'', β'', σ'' and χ'' intermolecular vibrations from those in reference 22 so that the agreement with the SCS-CC2/aVTZ harmonic frequencies is better. The frequencies and band assignments are listed in Table 3, together with the calculated S_0 state and experimental S_1 state frequencies.

4.4 Two-Color Resonant Two Photon Ionization Spectrum

The two-color resonant two-photon ionization spectrum of $(mCP)_2$ was recorded in the $33200 - 33850\ cm^{-1}$ region and is shown in Figure 5. The $S_0 \rightarrow S_1$ electronic origin is at 33255 cm^{-1}. Both

the position of the origin and the vibronic band positions agree within ± 1 cm^{-1} with those reported in ref. 22. The vibronic bands were assigned to based on the dispersed fluorescence spectrum (see Section 4.3)and on the calculated SCS-CC2/aVTZ frequencies. We have assigned the lowest-lying δ' and β' as well as the χ' and σ' vibrations oppositely to those in ref. 22, all other assignments are the same, and are listed in Table 3.

The fact that the δ'' vibrational fundamental, which transforms as a_g in C_i is discernible in the DF and is clear in the R2PI spectrum strongly suggests that the S_0 state structure is effectively C_i symmetric. As discussed in section 4.1, the $v'' = 1$ and higher levels of the δ'' vibration may be delocalized over the C_{2h} and both C_i structures. However, since the β vibration is non-totally symmetric (a_u) in C_i symmetry it should not appear as a fundamental, as is indeed the case for the DF spectrum, where β_0^1 does not appear but β_0^2 is observed. In the R2PI spectrum, we observe a weak band at $0_0^0 + 15.4$ cm^{-1}, which we tentatively ascribe to β_0^1. We have considered several possibilities why this fundamental does appear:

(1) Existence of several different S_0 state forms, as is predicted by the calculations. In this case, the R2PI spectra that originate from the ground state $v = 0$ levels of the different forms should be separable by UV/UV hole-burning spectroscopy. However, UV/UV holeburning spectra measured when burning at the origin band, shown as Figure S2 (Supplemental Information) did not reveal the presence of two (or more) separable v"$= 0$ species.

(2) Excited-state $(mCP)_2$ is effectively C_2-symmetric. While this would make the β' vibration totally symmetric (a), δ' then becomes non-totally-symmetric (b), leading to a problem in explaining the appearance of the δ' fundamental.

(3) Zehnacker and co-workers proposed a loss of symmetry upon electronic excitation which would lead to the appearance of the additional fundamentals.[22] Due to the excitonic coupling, the S_1 state adiabatic PES has a double-minimum shape along one or more antisymmetric vibrations.[24] While each of the adiabatic S_1 state minima have lower local symmetry (C_1), the molecular symmetry (MS) group of the coupled S_1/S_2 states remains C_i, and the symmetry-restriction rules still apply. The question of the (a)symmetry of the coupled S_1/S_2 excited states is discussed in detail

below.

(4) For intermolecular complexes of aromatics with noble-gas atoms, Felker and co-workers have shown that vibronic transitions which are nominally forbidden as fundamentals by rigid-molecule selection rules may nevertheless gain significant intensity if they involve intermolecular vibrations in which the aromatic moiety - which carries the electronic transition-dipole moment (TDM) - librates with sufficiently large amplitude, which renders such transitions vibronically active.[37] In $(mCP)_2$ the out-of-plane intermolecular bending vibration β' librationally modulates the electronic TDMs of both monomers, and this may render the β' fundamental active in the spectrum.

Considering the very small energy differences between the S_0 state minima discussed in Section 4, we expect the potential energy surface along the δ and β normal coordinates to be very flat. It is therefore probable that the lowest-frequency vibrations are delocalized over several ground state structures. The δ-mode interconnects the C_i-minima via the C_{2h}-structure, while the β-mode interconnects the two V-shape C_2 minima via the C_{2h}-structure. The δ mode is a_g in C_i and β is a in C_2 symmetry, respectively, but not in C_{2h}. On the other hand, their first overtone is fully allowed in all symmetries. This might explain the intensities of the measured spectrum: Both fundamental transitions are weak, while the corresponding overtones are much more intense.

5 Discussion

5.1 Excitonic Splitting and Isotope Effects

Isotopic substitution by even a single ^{13}C or a D atom breaks the inversion symmetry of $(mCP)_2$ strongly enough to render also the $S_0 \rightarrow S_2$ transition allowed. The 2C-R2PI spectra of both $^{12}C/^{13}C$-substituted and H/D-substituted dimers were measured, in order to break the dimer symmetry in two ways, allowing to measure two S_1/S_2 splittings. Figure 6(a) compares the origin region of *all*-^{12}C-$(mCP)_2$ to that of ^{13}C-$(mCP)_2$ in Figure 6(b). The ^{13}C-$(mCP)_2$ spectrum shows an additional weak band at 33264 cm^{-1}, about 8 cm^{-1} above the intense $S_0 \rightarrow S_1$ 0_0^0 transition at

33256 cm^{-1}. The former is assigned to the $S_0 \rightarrow S_2$ 0_0^0 transition, giving the excitonic splitting $\Delta_{obs,^{13}C} = 8.0 \pm 0.4$ cm^{-1}.

$^{12}C/^{13}C$ isotopic contribution: The changes in the zero-point vibrational energy (ZPVE) upon isotopic substitution lead to an $^{12}C/^{13}C$ isotopic shift of the 0_0^0 transition Δ_{iso} which contributes to the splitting. In the dimers (benzoic acid)$_2$ [14] and (benzonitrile)$_2$,[15] the analogous isotopic shifts were $\Delta_{obs^{13}C} = 3.3$ cm^{-1} and $\Delta_{obs^{13}C} = 3.9$ cm^{-1}, respectively. These small shifts may be treated by second-order degenerate perturbation theory, as $\Delta_{obs^{13}C} = \sqrt{\Delta_{exc}^2 + \Delta_{iso,^{13}C}^2}$. The $\Delta_{iso,^{13}C}$ contribution was determined by measuring the monomer 2C-R2PI spectra of mCP and ^{13}C-mCP. Figure 7 shows that the $S_0 \rightarrow S_1$ origin of ^{13}C-mCP is shifted by $+3.3 \pm 0.4$ cm^{-1} relative to that of mCP. Thus, the *purely excitonic* contribution Δ_{exc} to the splitting between the S_1 and S_2 origin bands is $\Delta_{exc} = \sqrt{\Delta_{obs,^{13}C}^2 - \Delta_{iso,^{13}C}^2} = 7.3 \pm 0.5$ cm^{-1}.

H/D isotope shift: Figure 6(c) shows the origin region of (mCP-*h*)(mCP-*d*). The intense $S_0 \rightarrow S_1$ 0_0^0 transition lies at 33260 cm^{-1}, here the weaker $S_0 \rightarrow S_2$ 0_0^0 band appears at 33270 cm^{-1}. The latter transition is more intense compared to of ^{13}C-(mCP)$_2$, which indicates a stronger symmetry breaking by H/D exchange as compared to $^{12}C/^{13}C$ substitution, and also a stronger exciton localization, see below. The observed S_1/S_2 splitting is $\Delta_{obs,D} = 10$ cm^{-1}, or 2 cm^{-1} larger than for the ^{13}C-isotopomer. H/D substitution changes the ZPVE than $^{12}C/^{13}C$ exchange, because the relative change of mass is much larger. The R2PI spectra of (mCP-*d*)(mCP-*h*) and (mCP-*d*)$_2$ are compared to that of (mCP)$_2$ in Figure 8. The R2PI spectrum of non-deuterated (mCP)$_2$ shown in Figure 8(a) shows the same vibronic structure as that of the doubly O-H/O-D deuterated homodimer (mCP-*d*)$_2$, Figure 8(c). However, in the (mCP-*d*)(mCP-*h*) heterodimer, the inversion symmetry is broken, rendering the R2PI spectrum much more complex as both the $S_0 \rightarrow S_1$ and $S_0 \rightarrow S_2$ transitions are allowed, giving rise to more vibronic bands, see Figure 8(b). The excitonic splitting $\Delta_{exc} = 7.3$ cm^{-1} determined above allows to extract $\Delta_{iso,D} = 6.8$ cm^{-1} from the observed splitting $\Delta_{obs,D}$ as $\Delta_{iso,D} = \sqrt{\Delta_{obs,D}^2 - \Delta_{exc}^2} = 10$ cm^{-1} as 6.8 cm^{-1}.

Vibronic quenching : To relate the observed excitonic splitting of $\Delta_{exc} = 7.3$ cm^{-1} to the calculated electronic Davydov-splitting Δ_{el} (e.g., 179 cm^{-1} with the SCS-CC2/aVTZ method), the latter must be reduced or "quenched" by the dimensionless vibronic quenching factor Γ_{vibron}, using Förster's perturbation theory ansatz:[13]

$$\Delta_{vibron} = \Delta_{el} \cdot \Gamma_{vibron}, \tag{11}$$

The vibronic quenching factor, $\Gamma_{vibron} = \prod_i exp(-S_i)$ is the product of the individual vibrational quenching factors $\gamma_i = exp(-S_i) \leq 1$, where i ranges over all totally-symmetric vibrational modes of the monomer and S_i is the i-th dimensionless vibrational displacement between the S_0 and S_1 state along the vibrational coordinate Q_i (Huang-Rhys factor). S_i is a measure for the intensity of the corresponding vibronic line and can be obtained (1) experimentally, from the intensities of totally-symmetric vibronic band fundamentals in the dispersed fluorescence spectrum of the mCP monomer, giving Γ^{exp}_{vibron};[15] (2) computationally from the κ_i coupling parameters of the monomer $S_0 \leftrightarrow S_1$ transition, as described in section 5.2, giving Γ^{calc}_{vibron};[15] (3) following a different computational path, Γ_{vibron} can be calculated via the effective-mode approximation, giving Γ^{eff}_{vibron}.[24]

Table 4 lists the mode-specific quenching factors γ_i of the mCP monomer and the total vibronic quenching factors Γ^{exp}_{vibron} and Γ^{calc}_{vibron}. After quenching the calculated Davydov splitting $\Delta_{el} =$ 179 cm^{-1} with Γ^{exp}_{vibron} (column 4 of Table 4) one obtains $\Delta^{exp}_{vibron} = 7.7$ cm^{-1}, which is in excellent agreement with the experimentally observed splitting $\Delta_{exc} = 7.3$ cm^{-1}. When quenching Δ_{el} with Γ^{calc}_{vibron}, we obtain $\Delta^{calc}_{vibron} = 24.2$ cm^{-1}; the same value is obtained upon quenching with Γ^{eff}_{vibron}. The latter two values are more than three times larger than experimentally observed. The reason for this can be seen in columns 2 and 3 of Table 4, which shows that many of the Huang-Rhys factors γ_i calculated for the $S_{\leftrightarrow}S_1$ transition of mCP are lower than the experimental ones.

5.2 Determination of the $(mCP)_2$ Coupling Parameters

The coupling constants necessary for the MCTDH simulation were obtained by taking the SCS-CC2/aVTZ C_i-symmetric ground state equilibrium geometry as reference geometry in the vibronic coupling formalism and subsequently distorting along every normal mode. The inter- and intrastate coupling constants (λ and κ) were determined from least squares fits of the analytical expressions for the adiabatic surfaces (Eqs. 5 and 6, omitting $\omega_{g/u}$) to the *ab initio* calculated excitation energies. This procedure has been successfully employed for the dimers of 2-pyridone and of *ortho*-cyanophenol.[16,18] The coupling parameters for the a_g and a_u normal modes with a frequency up to 600 cm^{-1} are listed in Tables 5 and 6, respectively. Modes marked by an asterisk are considered in the LVC and QVC simulations. The corresponding normal-mode eigenvectors are shown in Figures 9 and 10. The criterion for including a mode in the LVC and QVC simulations is that its frequency is smaller than 600 cm^{-1} and that its Huang-Rhys factor is $S_i > 0.02$.

Figure 11 shows the fits to the excitation energies along the selected a_g modes. The quadratic coupling constant γ is a measure of frequency change: A negative/positive curvature of the excitation energies indicates a frequency lowering/increase upon electronic excitation.[16] For the a_u vibrations, the coupling constants are calculated from fits to the sum and the difference of the adiabatic potential energy curves along the antisymmetric normal coordinates Q_u, shown in Figure 12. The curvature of the difference of the adiabatic PES is a measure of the linear coupling constant λ: The stronger the curvature, the larger λ.

5.3 Vibronic Spectrum Simulation

The simulation of the excited state vibronic spectrum was performed with the MCTDH program package[38] using the linear (LVC) and quadratic (QVC) vibronic coupling models. Both simulations are shown in Figure 13(b) and (c) along the experimental spectrum, Figure 13(a), in the spectral region up to 600 cm^{-1}. All spectra are set to a common origin. The simulations include seven totally-symmetric (a_g) and five a_u modes. The corresponding coupling constants are collected in Tables 5 and 6. We account for the higher-frequency modes by introducing a prequenched

energy gap of 59.0 cm^{-1} between the two electronic states, which is determined by treating the high-frequency coupling modes within Förster's perturbation theory approach. For details on the prequenching, see ref. 18; the prequenching concept has successfully been applied to the dimers of *ortho*-cyanophenol and 2-pyridone.[16,18] In all cases, the ground state potentials are taken to be harmonic with frequencies $\omega_{g/u}$. The LVC simulation only contains the linear coupling parameters κ and λ, while the QVC calculation additionally includes the quadratic coupling parameters γ. For mode ν_1 we introduce an exception in the QVC simulation. In this case the combination of the harmonic ground state with the quadratic coupling terms would lead to an unphysical behavior of the PES (unbound from below). To stay in line with our model approach we therefore neglect the quadratic coupling terms for mode ν_1. The initial wave function is chosen as a product of harmonic oscillator functions. The line assignments for the LVC and QVC spectra are collected in Table 7 and are based on the nodal structures of the respective vibronic densities.

In the LVC simulation shown in Figure 13(b), the calculated frequencies are close to the experimentally observed ones shown in Figure 13(a), especially below 400 cm^{-1}, see also Table 3. The intensities of the stagger (δ) and in-plane nitrogen-bend (δCC-N) are well reproduced. The intensities of the σ transitions are underestimated by the simulation compared to the experiment. The same applies to χ. It may be due to the different ground state structures present that the transitions of σ and χ are larger in the experimental spectrum, as these vibrations are totally-symmetric for all geometries. Also, the band intensities of R2PI spectra are not as reliable as for example the intensities of DF spectra, because they are sensitive to temperature and saturation effects. Nonetheless, the structure of the simulated spectrum shows a similarity to the observed spectrum, although fewer bands could be reproduced, especially in the low-energy region. In the high-energy region, $6a_0^1$ shows combinations with δ_0^1, σ_0^1 and χ_0^1, which agrees well with experiment. The intensity of $6a_0^1$ is overestimated. In general, the frequencies in the spectrum above 400 cm^{-1} are not well reproduced by the LVC simulation and the intensities are overestimated.

The QVC simulation in Figure 13(c) shows intensities closer to experiment in the low-energy region compared to the LVC spectrum, especially for the σ bands. The $6a_0^1$ intensity is overes-

timated, while the intensity of δCC-N$_0^1$ and $6b_0^1$ are very reasonable. Also, the frequencies have changed markedly. For the higher energy region of the spectrum ($\geq$400 cm^{-1}), the frequencies of the QVC simulation are closer to the R2PI spectrum than the LVC frequencies. However, for the low-energy region the opposite is the case: Most frequencies are somewhat too small in the QVC simulation, although the deviation to experiment is reduced compared to the LVC results.

While the frequencies for the totally symmetric modes in the calculated spectra well match the harmonic ground state frequencies, for the coupling modes ω, δC-OH$_{as}$ and 6a$_{as}$ the frequencies for excitation of one quantum are larger in the LVC model than the ground state frequency. In the QVC scheme, this increase is compensated by the negative quadratic coupling constants. Regarding symmetry selection rules, the excitation of odd quanta in the coupling modes should not be observed. However, they appear because, due to the coupling of the electronic S_1 and S_2 states, the vibronic wave functions have components associated with both electronic states. As demonstrated earlier, this results in non-adiabatic effects and may lead to complicated spectral features.[16,18]

The overall shape of the spectrum is reproduced although certain bands of the out-plane vibrations are missing in the simulation because the Huang-Rhys factor is too small. As discussed previously, the use of Cartesian displacement coordinates can be problematic for the low-frequency out-of-plane modes.[16] Table 7 gives an overview over the observed and simulated frequencies for the LVC and QVC model.

The extremely small Huang-Rhys factors of out-of-plane modes (see Tables 5 and 6) indicate that the coupling parameters may not be of good quality. The displacement around the equilibrium geometry ($Q = 0$) is performed along the Cartesian normal-mode eigenvectors of every vibration. Especially at large displacements this may lead to incorrect bond length changes. This problem can be overcome by employing internal coordinates, rather than the Cartesian normal-mode eigenvectors. This has the advantage that no bond length changes are mixed into angular deformations, but is beyond the scope of this work.

5.4 Localization of the Excitation

The localization of the excitation in the different species is determined in the same way as for (benzoic acid)$_2$ and (benzonitrile)$_2$.[14,15] For both homodimers (mCP-*h*)$_2$ and (mCP-*d*)$_2$, only the $S_0 \rightarrow S_1$ transition is observed, see Figure 8. Therefore, the excitation is fully delocalized over both monomers. Breaking the inversion symmetry leads to a partial localization.[14,15] Degenerate perturbation theory allows to determine the localization of the wave functions by means of the mixing angle α, which is defined as $tan(2\alpha) = |\Delta_{exc}|/|E_{A^*B} - E_{AB^*}|$;[19] for details, see refs. 14 and 15.

First we consider the ^{13}C-isotopomer, where $\alpha = 21.1°$. Therefore, Ψ^+ is 86% localized on monomer *A* (^{12}C-mCP) and only 14% on monomer *B* (^{13}C-mCP), and vice versa for Ψ^-. For (mCP-*h*)(mCP-*d*) $\alpha = 18.1°$, leading to Ψ^+ being 90% localized on monomer *A* (mCP-*h*) and 10% localized on monomer *B* (mCP-*d*), and again vice versa for Ψ^-. These ratios can be compared to experimental observations via the dimer oscillator strengths $f^{\pm}_{dim}$, see refs. 14 and 15. For ^{13}C-(mCP)$_2$, a calculated ratio of $f^+_{dim} : f^-_{dim} = 1 : 0.19$ results. The integrated intensities of the experimental $S_0 \rightarrow S_1$ and $S_0 \rightarrow S_2$ origins shown in Figure 6 are in good agreement, being 1 : 0.10. This indicates that the determined isotopic and excitonic contributions are reliable. From the determined splitting in (mCP-*h*)(mCP-*d*), the calculated intensity ratio is $f^+_{dim} : f^-_{dim} = 1 : 0.26$; the experiment yields 1 : 0.30, in excellent agreement. Consequently, the ^{13}C-substitution leads to a smaller localization of the excitation compared to partial deuteration of mCP. Nevertheless, in both heterodimers the monomers are distinguishable in the excited state. The excitation can oscillate back and forth between the monomers upon excitation with a large enough bandwidth to cover both origins.[19]

For the homodimers (mCP)$_2$ and (mCP-*d*)$_2$ the angle is $\alpha = \pi/4$; the semiclassical exciton transfer rate is $k_{AB} = 4|V_{AB}|/h = 2|\Delta_{exc}| \cdot c$,[19] resulting in a transfer rate of $k_{AB} = 4.4 \cdot 10^{11}$ s^{-1}, which is equivalent to an exciton hopping time of $t_{exc} = (k_{AB})^{-1} = 2.3$ ps. This is much faster compared to the benzoic acid dimer (17.7 ps)[14] and the benzonitrile dimer (8.0 ps).[15] A possible reason is the much smaller intermolecular distance: $R_{AB} = 5.34$ Å for (mCP)$_2$, while in (BZA)$_2$

and $(BN)_2$ the monomers are 7.14 Å and 6.53 Å apart, respectively.[14]

For the heterodimers, the excitation is partially localized, therefore the transfer rate should decrease and the hopping time increase compared to the electronically delocalized homodimers. The transfer rate of ^{13}C-$(mCP)_2$ is determined to be $k_{AB} = 1.6 \cdot 10^{11}$ s^{-1}, corresponding to $t_{exc} =$ 6.3 ps. The increase in hopping time is very small compared to $(mCP)_2$, agreeing with a partial localization. For (mCP-*h*)(mCP-*d*), the transfer rate is $k_{AB} = 7.1 \cdot 10^{10}$ s^{-1}. The decrease in k_{AB} is a bit larger compared to the ^{13}C-$(mCP)_2$. The hopping time is therefore a little longer, $t_{exc} = 14$ ps. Thus, the excitation is slightly more localized in (mCP-*h*)(mCP-*d*) compared to ^{13}C-$(mCP)_2$.

5.5 Asymmetry of the First Excited State

Due to the appearance of the out-of-plane fundamental β_0^1, Seurre *et al.* suggested a symmetry loss upon excitation breaking the inversion center.[22] Based on this they concluded a localization of the excitation on the monomers. The S_1 state geometry optimization of $(mCP)_2$ shows indeed an asymmetric deformation. Both rings expand upon excitation, but the C-C bond lengths in monomer *A* increase by $28 - 54$ pm, while they increase only by $12 - 14$ pm in monomer *B*. This leads to a C_1 symmetry. Table 8 details the bond lengths and structure parameters of the S_0 and S_1 states.

For symmetry reasons, there is a second dimer structure, in which the deformations on *A* and *B* are exchanged. This structure corresponds to the symmetry-equivalent and degenerate minimum of the double-well type S_1 adiabatic potential of $(mCP)_2$. Both the S_1 and S_2 states of the dimer are delocalized over both minima, therefore, the geometry change does not imply localization of the excitation in an asymmetric structure. This is illustrated by the adiabatic PESs of the first and second excited state along the antisymmetric effective mode coordinate Q_-^{eff} in Figure 14. The aspect of localization in case of isotopic substitution is treated above in detail.

6 Conclusions

The S_1/S_2 excitonic splitting of the C_i-symmetric dimer (*meta*-cyanophenol)$_2$ is not directly measurable by optical spectroscopy, because its $S_0 \rightarrow S_1$ ($A_g \rightarrow A_u$) transition is electric-dipole allowed, while the $S_0 \rightarrow S_2$ ($A_g \rightarrow A_g$) transition is dipole-forbidden. A single ^{12}C/^{13}C or H/D substitution breaks the inversion symmetry of (mCP)$_2$ sufficiently to render the $S_0 \rightarrow S_2$ transition somewhat allowed. We have measured mass-selected two-color resonant two-photon ionization spectra of the $S_0 \rightarrow S_1$ and $S_0 \rightarrow S_2$ electronic origins of ^{12}C/^{13}C or H/D substituted dimers of mCP. Combining the information of the ^{13}C-(mCP)$_2$ and (mCP-*h*)(mCP-*d*) heterodimer spectra allows to experimentally determine the excitonic splitting of (mCP)$_2$ as $\Delta_{exc} = 7.3$ cm^{-1}.

CC2 and SCS-CC2 calculations predict three close-lying ground-state structures of (mCP)$_2$: The lowest is near-planar but slightly Z-shaped (C_i-symmetric, two enantiomers), the second-lowest structure is $0-5$ cm^{-1} higher and is planar and C_{2h}-symmetric. The third structure is $3-11$ cm^{-1} higher and is V-shaped (C_2-symmetric, two enantiomers). CC2 and SCS-CC2/aVDZ calculations predict a π-stacked dimer geometry, which is $270-470$ cm^{-1} higher; this structure is not a minimum at the SCS-CC2/aVTZ level.

The isotope-dependent shifts in the $S_0 \rightarrow S_1/S_2$ origin bands of the ^{13}C-(mCP)$_2$ and (mCP-*h*)(mCP-*d*) heterodimers arise from the changes of the vibrational zero-point energy between the electronic ground and excited states. The isotope shift that arises from a single ^{12}C/^{13}C substitution was determined as $\Delta_{iso,^{13}C} = 3.3$ cm^{-1}; we do not observe any dependence on the position of the ^{13}C atom within the dimer, although there must be small effects. The isotope effect that arises from H/D exchange in the phenolic OH group is somewhat larger, being $\Delta_{iso,D} = 6.8$ cm^{-1}. This leads to a larger splitting between the vibrationless levels of the S_1 and S_2 states.

The purely electronic (vertical) excitonic splitting calculated with the SCS-CC2 method and the aug-cc-pVTZ basis set is $\Delta_{el} = 179$ cm^{-1}. The large difference between this value and the experimental $\Delta_{exc} = 7.3$ cm^{-1} reflects the importance of vibronic coupling, which reduces or quenches the purely electronic splitting. The vibronic quenching factor $\Gamma_{vibron} = \Pi_i \gamma_i$ that is experimentally determined from the mCP dispersed fluorescence spectrum, $\Gamma_{vibron}^{exp} = 0.043$, yields

$\Delta^{exp}_{vibron} = \Delta_{el} \cdot \Gamma^{exp}_{vibron} = 7.7$ cm^{-1}, in very good agreement with the experiment. The quenching factor Γ^{calc}_{vibron} derived from the mCP monomer calculated $S_0 \rightarrow S_1$ spectrum is three times larger, resulting in a $\Delta^{calc}_{vibron} = 24.2$ cm^{-1}.

Our conclusion that the excitonic excitations are delocalized is in disagreement with the interpretation of Seurre *et al.*,[22] but not with their experimental observations. The excitonic coupling between S_1 and S_2 gives rise to two asymmetric S_1 state minimum-energy geometries, corresponding to a potential with two symmetry-equivalent minima along the antisymmetric effective mode coordinate Q^{eff}_{-}. While the rigid-molecule symmetry at these minima is reduced from C_i to C_1, the molecular symmetry (MS) group of the S_1 state including tunneling remains C_i(M).[15–18]

We interpret the appearance of the fundamental of the low-frequency out-of-plane mode β' in the $S_0 \rightarrow S_1$ spectra as deriving from the strongly librational character of the β vibration, which modulates the electronic TDM strongly enough to induce the appearance of fundamental transitions in this nominally antisymmetric mode by a Herzberg-Teller-like mechanism.[37]

The simulation of the vibronic spectrum with MCTDH agrees fundamentally with the structure of the in-plane modes observed experimentally. Issues arose for the description of out-of-plane modes, as the predicted Huang-Rhys parameters were far too small to cause these modes to appear in the spectrum. Apparently, the geometry displacement along the normal-mode eigenvectors is not the best description and internal coordinates would be necessary for a complete description and simulation of the out-of-plane modes. Nevertheless, the simulations agrees with the observed spectrum and differences of linear and quadratic vibronic coupling have been illustrated.

Acknowledgments

This work was supported by the Schweiz. Nationalfonds (project nos. 200020-152816 and 132540) and the Deutsche Forschungsgemeinschaft (project no. AZ KO945/17-1).

Supporting Information Available: Figure S1 with the C_2-symmetric, stacked structure of the meta-cyanophenol dimer (not observed experimentally). Figure S2 with UV/UV-holeburned spec-

trum, Tables S1 to S4 with Cartesian coordinates of the SCS-CC2/aug-cc-pVTZ optimized four structures in Table 1.

References

(1) Cheng, Y. C.; Fleming, G. Dynamics of Light Harvesting in Photosynthesis. *Annu. Rev. Phys. Chem.* **2009**, *60*, 241–262.

(2) Novoderezhkin, V. I.; van Grondelle, R. Physical Origins and Models of Energy Transfer in Photosynthetic Light-Harvesting. *Phys. Chem. Chem. Phys.* **2010**, *12*, 7352–7365.

(3) Strümpfer, J.; Schulten, K. Excited State Dynamics in Photosynthetic Reaction Center and Light Harvesting Complex 1. *J. Chem. Phys.* **2012**, *137*, 065101–1–7.

(4) Fassioli, F.; Dinshaw, R.; Arpin, P. C.; Scholes, G. D. Photosynthetic Light Harvesting: Excitons and Coherence. *J. Roy. Soc. Interface* **2014**, *11*, 20130901–1–22.

(5) Scholes, G. D.; Smith, C. Detecting and Measuring Exciton Delocalization in Photosynthetic Light Harvesting. *J. Chem. Phys.* **2014**, *140*, 110901–1–8.

(6) Spano, F. C. Excitons in Conjugated Oligomer Aggregates, Films, and Crystals. *Annu. Rev. Phys. Chem.* **2006**, *57*, 217–243.

(7) Markovitsi, D.; Onidas, D.; Gustavsson, T.; Talbot, F.; Lazzarotto, E. Collective Behavior of Franck-Condon Excited States and Energy Transfer in DNA Double Helices. *J. Am. Chem. Soc.* **2005**, *127*, 17130–17131.

(8) Middleton, C. T.; de La Harpe, K.; Su, C.; Law, Y. K.; Crespo-Hernandez, C. E.; Kohler, B. DNA Excited-State Dynamics: From Single Bases to the Double Helix. *Annu. Rev. Phys. Chem.* **2009**, *60*, 217–239.

(9) Müller, A.; Talbot, F.; Leutwyler, S. S_1/S_2 Exciton Splitting in the (2-Pyridone)$_2$ Dimer. *J. Chem. Phys.* **2002**, *116*, 2836–2847.

(10) Ottiger, P.; Leutwyler, S.; Köppel, H. S_1/S_2 Excitonic Splittings and Vibronic Couplings in the Excited-State of the Jet-Cooled 2-Aminopyridine Dimer. *J. Chem. Phys.* **2009**, *131*, 204308–1–11.

(11) Ottiger, P.; Leutwyler, S. Excitonic Splittings in Jet-Cooled Molecular Dimers. *CHIMIA* **2011**, *65*, 228–230.

(12) Heid, C. G.; Ottiger, P.; Leist, R.; Leutwyler, S. The S_1/S_2 Exciton Interaction in 2-Pyridone·6-Methyl-2-Pyridone: Davydov Splitting, Vibronic Coupling and Vibronic Quenching Effects. *J. Chem. Phys.* **2011**, *135*, 154311–1–15.

(13) Ottiger, P.; Leutwyler, S.; Köppel, H. Vibrational Quenching of Excitonic Splittings in H-Bonded Molecular Dimers: The Electronic Davydov Splittings Cannot Match Experiment. *J. Chem. Phys.* **2012**, *136*, 174308–1–13.

(14) Ottiger, P.; Leutwyler, S. Excitonic Splitting and Coherent Electronic Energy Transfer in the Gas-Phase Benzoic Acid Dimer. *J. Chem. Phys.* **2012**, *137*, 204303.

(15) Balmer, F. A.; Ottiger, P.; Leutwyler, S. Excitonic Splitting, Delocalization, and Vibronic Quenching in the Benzonitrile Dimer. *J. Phys. Chem. A* **2014**, *118*, 11253–11261.

(16) Kopec, S.; Ottiger, P.; Leutwyler, S.; Köppel, H. Analysis of the $S_2 \leftarrow S_0$ Vibronic Spectrum of the ortho-Cyanophenol Dimer Using a Multimode Vibronic Coupling Approach. *J. Chem. Phys.* **2015**, *142*, 084308–1–16.

(17) Ottiger, P.; Köppel, H.; Leutwyler, S. Excitonic Splittings in Molecular Dimers: Why Static Ab Initio Calculations Cannot Match Them. *Chem. Sci* **2015**, *6*, 6059–6068.

(18) Kopec, S.; Köppel, H. Theoretical Analysis of the $S_0 \rightarrow S_2$ Vibronic Spectrum of the 2-Pyridone Dimer. *J. Chem. Phys.* **2016**, *144*, 024314–1–13.

(19) Förster, T. In *Modern Quantum Chemistry*; Sinanoglu, O., Ed.; Academic Press, New York, 1965; Chapter III. B, p 93.

(20) Fulton, R. L.; Gouterman, M. Vibronic Coupling. I. Mathematical Treatment for Two Electronic States. *J. Chem. Phys.* **1961**, *35*, 1059–1071.

(21) Fulton, R. L.; Gouterman, M. Vibronic Coupling. II. Spectra of Dimers. *J. Chem. Phys.* **1964**, *41*, 2280–2286.

(22) Seurre, N.; Barbu-Debus, K. L.; Lahmani, F.; Zehnacker-Rentien, A.; Sepiol, J. Electronic and Vibrational Spectroscopy of Jet-Cooled m-Cyanophenol and its Dimer: Laser-Induced Fluorescence and Fluorescence-Dip IR Spectra in the S_0 and S_1 states. *Chem. Phys.* **2003**, *295*, 21–33.

(23) Köppel, H.; Domke, W.; Cederbaum, L. S. Multimode Molecular Dynamics Beyond the Born-Oppenheimer Approximation. *Adv. Chem. Phys.* **1984**, *57*, 59–245.

(24) Kopec, S.; Ottiger, P.; Leutwyler, S.; Köppel, H. Vibrational Quenching of Excitonic Splittings in H-Bonded Molecular Dimers: Adiabatic Description and Effective Mode Approximation. *J. Chem. Phys.* **2012**, *137*, 184312–1–10.

(25) Nebgen, B.; Emmert, F. L.; Slipchenko, L. V. Vibronic Coupling in Asymmetric Bichromophores: Theory and Application to Diphenylmethane. *J. Chem. Phys.* **2012**, *137*, 084112–1–12.

(26) Nebgen, B.; Slipchenko, L. V. Vibronic Coupling in Asymmetric Bichromophores: Theory and Application to Diphenylmethane-d5. *J. Chem. Phys.* **2014**, *141*, 134119–1–9.

(27) Pillsbury, N. R.; Kidwell, N. M.; Nebgen, B.; Slipchenko, L. V.; Douglass, K. O.; Cable, J. R.; Plusquellic, D. F.; Zwier, T. S. Vibronic Coupling in Asymmetric Bichromophores: Experimental Investigation of Diphenylmethane-d_5. *J.Chem. Phys.* **2014**, *141*, 064316–1–9.

(28) Meyer, H.-D.; Manthe, U.; Cederbaum, L. S. The Multi-Configurational Time-Dependent Hartree Approach. *Chem. Phys. Lett.* **1990**, *165*, 73–78.

(29) Meyer, H.-D.; Gatti, F.; Worth, G. A. *Multidimensional Quantum Dynamics: MCTDH Theory and Application*; Wiley-VCH, 2009.

(30) Beck, M. H.; Jäckle, A.; Worth, G. A.; Meyer, H.-D. The Multiconfigurational Time-Dependent Hartree (MCTDH) Method: A Highly Efficient Algorithm For Propagating Wavepackets. *Phys. Rep.* **2000**, *324*, 1–105.

(31) Hättig, C.; Weigend, F. CC2 Excitation Energy Calculations on Large Molecules using the Resolution of the Identity Approximation. *J. Chem. Phys.* **2000**, *113*, 5154–5161.

(32) Hättig, C. Geometry Optimizations with the Coupled-Cluster Model CC2 using the Resolution of the Identity Approximation. *J. Chem. Phys.* **2003**, *118*, 7751–7761.

(33) Hellweg, A.; Grün, S. A.; Hättig, C. Benchmarking the Performance of Spin-component Scaled CC2 in Ground and Electronically Excited States. *Phys. Chem. Chem. Phys.* **2008**, *10*, 4119–4127.

(34) Winter, N.; Graf, N. K.; Leutwyler, S.; Hättig, C. Benchmarks for 0-0 Transitions of Aromatic Organic Molecules: DFT/B3LYP, ADC(2), CC2, SOS-CC2 and SCS-CC2 Compared to High-Resolution Gas-Phase Data. *Phys. Chem. Chem. Phys.* **2013**, *15*, 6623–6630.

(35) TURBOMOLE *V6.3 2011*; a development of Universität Karlsruhe (TH) and Forschungszentrum Karlsruhe GmbH, 1989-2007, TURBOMOLE GmbH; available from `http://www.turbomole.com`.

(36) The thresholds for SCF and one-electron density convergence were set to 10^{-9} a.u. and 10^{-8} a.u., respectively. The convergence thresholds for all structure optimizations were set to 10^{-8} a.u. for the energy change, $6 \cdot 10^{-6}$ a.u. for the maximum displacement element,

10^{-6} a.u. for the maximum gradient element, $4 \cdot 10^{-6}$ a.u. for the RMS displacement and 10^{-6} a.u. for the RMS gradient.

(37) Maxton, P. M.; Schaeffer, M. W.; Ohline, S. M.; Kim, W.; Venturo, V.; Felker, P. M. The Raman and Vibronic Activity of Intermolecular Vibrations in Aromatic-Containing Complexes and Clusters. *J. Chem. Phys.* **1994**, *101*, 8391–8408.

(38) Worth, G. A.; Beck, M. H.; Jäckle, A.; Meyer, H.-D. The MCTDH Package, Version 8.4. 2007; University of Heidelberg, Heidelberg, Germany. http://mctdh.uni-hd.de.

Table 1: Calculated Relative Energies (in cm^{-1}) of the Four Lowest-Energy (*m*-Cyanophenol)$_2$ Structures, see Figure 2.

	Z-shaped C_i	Planar C_{2h}	V-shaped C_2	π-Stacked [a] C_2
CC2/aug-cc-pVDZ	0.0	0.0	11.3	474.4
CC2/aug-cc-pVTZ	0.0	5.5[b]	7.5	315.9
SCS-CC2/aug-cc-pVDZ	0.0	0.0	11.4	272.6
SCS-CC2/aug-cc-pVTZ	0.0	0.1	3.1	–

[a] shown in Figure S1 (Supplemental Information).
[b] index-1 saddle point

Table 2: Calculated Vertical Excitation Energies and Davydov-splitting Energies Δ_{el} (in cm^{-1}) of the H-bonded (*m*-Cyanophenol)$_2$ Structures, see Figure 2.

		CC2/aVDZ		**CC2/aVTZ**		**SCS-CC2/aVDZ**		**SCS-CC2/aVTZ**	
Z-shaped (C_i)	Irred.	E_{exc}	f_{el}	E_{exc}	f_{el}	E_{exc}	f_{el}	E_{exc}	f_{el}
S_1	A_u	35369	0.157	35849	0.160	35412	0.123	35935	0.134
S_2	A_g	35563	0.000	36045	0.000	35585	0.000	36114	0.000
Δ_{el}		194		196		173		179	
Planar (C_{2h})									
S_1	B_u	35369	0.157	35845	0.160	35411	0.123	35935	0.134
S_2	A_g	35562	0.000	36046	0.000	35585	0.000	36115	0.000
Δ_{el}		193		201		174		180	
V-shaped (C_2)									
S_1	B	35370	0.157	35187	0.152	35412	0.123	35936	0.134
S_2	A	35562	$4 \cdot 10^{-4}$	35379	$4 \cdot 10^{-4}$	35585	$3 \cdot 10^{-4}$3E-04	36115	$3 \cdot 10^{-4}$
Δ_{el}		194		192		173		179	

Table 3: Experimental S_0 and S_1 Frequencies (in cm^{-1}) of (*m*-Cyanophenol)$_2$ and SCS-CC2/aug-cc-pVTZ S_0 Frequencies and Comparison to Assignments of Ref. 22.

Vibration S_1	2C-R2PI	Ref. 22(S_1)	Vibration S_0	Fluorescence	SCS-CC2/aVTZ	Ref. 22(S_0)
δ_0^1	12.8	30	δ_1^0	15	11	34
β_0^1	15.4	12	β_1^0	(17.5)[a]	13	11
δ_0^2	27.3		β_2^0	35		
β_0^2	30.4		σ_1^0	75	79	104
β_0^4	60.8		χ_1^0	103	109	75
θ_0^2	70.6		$\delta_1^0\chi_1^0$	119		
σ_0^1	84.5	75	σ_2^0	148		
$\sigma_0^1\ \delta_0^1$	97.3		δCC-N$_1^0$	168	171	165
$\theta_0^2\ \delta_0^2$	99.3					
$\sigma_0^1\ \delta_0^2$	111.2					
χ_0^1	116.9	84				
$\chi_0^1\ \delta_0^1$	127.6					
σ_0^2	167.1					
δCC-N$_0^1$	176.7					
$\sigma_0^2\ \delta_0^1$	180.0					
$\sigma_0^2\ \delta_0^2$	193.8					
χ_0^2	225.8					
σ_0^3	248.4					
$\sigma_0^3\ \delta_0^1$	263.4					
$\sigma_0^3\ \delta_0^2$	275.0					
δC-OH$_0^1$	394.9					
δC-OH$_0^1\delta_0^1$	407.6					
$6a_0^1$	413.5					
$6a_0^1\ \delta_0^1$	425.0					
$6a_0^1\ \beta_0^1$	430.8					
$6a_0^1\ \delta_0^2$	439.4					
δC-OH$_0^1\sigma_0^1$	478.5					
$6b_0^1$	496.6					
$6a_0^1\ \sigma_0^1$	498.8					
δC-CN$_0^1$	523.5					
$6a_0^1\ \chi_0^1$	529.8					
$6a_0^1\sigma_0^2$	578.0					
$6b_0^1\sigma_0^1$	582.6					

Frequency from the first overtone.

Table 4: SCS-CC2/cc-pVTZ calculated and experimental frequencies (in cm^{-1}) of the totally-symmetric vibrations of *m*-cyanophenol, calculated and experimental mode-specific quenching factors $\gamma_i = exp(-S_i)$, calculated and experimental total quenching factors Γ_{vibron}^{calc} and Γ_{vibron}^{exp}.

SCS-CC2/cc-pVTZ		Experimental	
Frequency/cm^{-1}	$\gamma_{i,calc}$ [a]	Freq. / cm^{-1}	$\gamma_{i,exp}$ [b]
141.8	0.975	146.5	0.942
387.4	0.991		
450.9	0.652	453.2	0.439
527.7	0.817	531.2	0.637
558.2	0.975	564.1	0.960
720.7	0.887	718.0	0.867
942.5	0.942	935.7	0.842
1003.9	0.660	1004.4	0.446
1093.8	0.977	993.7	0.900
1167.4	0.924		
1180.0	0.993		
1195.5	0.995		
1299.4	0.856	1286.5	0.591
1339.4	0.931		
1436.2	0.993		
1466.0	0.950		
1517.8	0.997		
1629.7	0.999		
1634.1	0.988		
2106.2	0.904		
3201.2	0.950		
3214.6	0.989		
3231.3	0.993		
3239.9	0.982		
3793.4	0.893		
Γ_{calc}	0.135	Γ_{exp}	0.0434
Δ_{vibron}^{calc}	24.2 cm^{-1}	Δ_{vibron}^{calc}	7.7 cm^{-1}

[a] from calculated coupling constants of mCP.
[b] from fluorescence band intensities of mCP.

Table 5: Vibronic coupling parameters (in cm^{-1}) based on SCS-CC2/aVTZ excited state potential fits for totally symmetric a_g modes. The mode number corresponds to the Turbomole numbering, for spectral reference the Wilson nomenclature is given in parenthesis. ω_g is the calculated frequency, κ the intrastate coupling constant, γ the quadratic coupling parameter and S_i the Huang-Rhys factor.

a_g-Mode	ω_g	State	κ	γ	S_i
1* (δ)	10.8	S_1	−4.8	−459.4	0.100
		S_2	1.0	−463.0	0.004
4* (σ)	79.2	S_1	55.1	−9.7	0.242
		S_2	49.6	−9.9	0.196
6* (χ)	108.5	S_1	−30.3	−14.5	0.039
		S_2	−27.3	−14.3	0.032
7	139.2	S_1	−4.5	−63.2	0.001
		S_2	−4.7	−63.2	0.001
9* (δCC-N)	171.4	S_1	79.9	−43.8	0.109
		S_2	73.5	−43.1	0.092
11	221.7	S_1	−3.5	−42.4	1.2E-04
		S_2	−3.9	−44.9	1.6E-04
13	381.1	S_1	2.7	−168.5	2.5E-05
		S_2	3.4	−168.7	3.9E-05
16 (δC-OH)	412.7	S_1	−21.7	−2.6	0.001
		S_2	−27.3	−3.5	0.002
18* (6a)	458.2	S_1	321.1	−34.5	0.246
		S_2	319.7	−35.7	0.243
19	460.5	S_1	36.1	−66.8	0.003
		S_2	36.0	−70.6	0.003
21* (6b)	528.4	S_1	229.1	−34.4	0.094
		S_2	208.8	−35.7	0.078
23* (δC-CN)	569.4	S_1	−136.3	−0.3	0.029
		S_2	−132.3	−1.3	0.027

Table 6: Vibronic coupling parameters (in cm^{-1}) based on SCS-CC2/aVTZ excited state potential fits for non-totally symmetric modes of a_u symmetry. The mode number corresponds to the Turbomole numbering, for spectral reference the Wilson nomenclature is given in parenthesis. ω_u is the calculated frequency, λ the interstate coupling constant, γ the quadratic coupling parameter and S_i the Huang-Rhys factor.

a_u-Mode	ω_u	λ	γ_1	γ_2	S_i
2 (β)	13.0	0.03	−377.0	−373.6	1.9E-06
3 (θ)	47.2	0.05	−21.7	−23.4	5.2E-07
5* (ω)	99.5	35.4	−52.6	−38.2	0.063
8	143.6	0.6	−61.4	−61.4	7.6E-06
10 (δCC-N$_{as}$)	183.8	12.0	−30.2	−30.3	0.002
12	224.2	0.1	−44.2	−45.1	9.5E-08
14	382.3	8.3	−170.0	−170.0	2.4E-04
15* (δC-OH$_{as}$)	412.1	117.9	−7.4	−2.3	0.041
17* (6a$_{as}$)	458.2	298.0	−33.9	−33.8	0.212
20	465.3	2.1	−69.0	−71.9	1.0E-05
22* (6b$_{as}$)	528.5	204.5	−35.1	−35.2	0.075
24* (δC-CN$_{as}$)	571.8	113.9	−3.7	6.8	0.020

Table 7: Vibrational frequencies (in cm^{-1}) in the experimental 2C-R2PI spectrum and in the linear (LVC) and quadratic (QVC) MCTDH simulations.

Vibration	2C-R2PI	LVC	QVC
δ_0^1	12.8	10.8	10.7
σ_0^1	84.5	79.2	74.2
$\sigma_0^1\delta_0^1$	97.3	90.0	85.0
χ_0^1	116.9	108.5	101.0
ω_0^1		128.9	93.3
σ_0^2	167.1	158.5	148.3
δCC-N$_0^1$	176.7	171.4	148.0
$\sigma_0^1\chi_0^1$		187.8	175.2
$\sigma_0^1\omega_0^1$		208.0	167.5
$\sigma_0^1\delta$CC-N$_0^1$		250.6	222.1
$\chi_0^1\delta$CC-N$_0^1$		279.9	249.1
$\omega_0^1\delta$CC-N$_0^1$			241.4
δC-OH$_{as}$		442.3	435.3
6a$_0^1$	413.5	458.5	440.8
6a$_0^1\delta_0^1$	425.0	469.4	451.5
(6a$_{as}$)$_0^1$		479.0	457.8
6b$_0^1$	496.6	528.4	511.1
6a$_0^1\sigma_0^1$	498.5	537.8	514.9
δC-CN$_0^1$	523.5	569.6	569.4

Table 8: Characteristic structure parameters (in Å) of (*meta*-cyanophenol)$_2$ in the SCS-CC2/aVTZ optimized S_0 and S_1 states. N' stands for the N atom of *B*.

Parameter	$S_0(C_i)$	$S_1(C_1)$	
	A = B	A	B
r(C_1-C_2)	1.397	1.443	1.410
r(C_2-C_3)	1.403	1.435	1.416
r(C_3-C_4)	1.394	1.431	1.407
r(C_4-C_5)	1.398	1.426	1.410
r(C_4-C_5)	1.399	1.453	1.412
r(C_5-C_6)	1.402	1.446	1.416
r(C_6-C_7)	1.437	1.419	1.449
r(C_7-N_8)	1.176	1.200	1.190
r(C_9-O_{10})	1.356	1.349	1.365
r(O_{10}-H_{11})	0.976	0.991	0.982
δ(C_6-C_7-N_8)	174.7°	173.2°	174.6°
δ(C_9-O_{10}-H_{11})	110.2°	110.8°	110.2°
r($H_{11}\cdots N'_8$)	2.025	1.978	
r($H_{11}\cdots N'_8$)	2.025	1.914	
R_{COM}	5.340	5.341	
Δ_z	0.006	0.004	

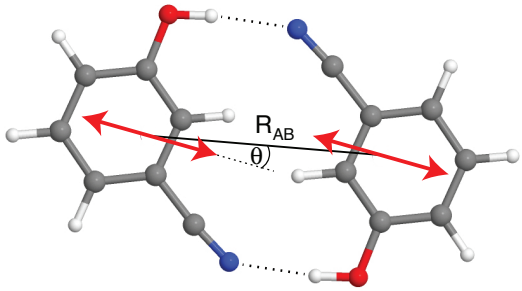

Figure 1: SCS-CC2/aug-cc-pVTZ structure and electronic transition dipole moment (TDM) directions of (*meta*-cyanophenol)$_2$. The distance between the centers of mass is $R_{AB} = 5.34$ Å, the angle between the intermonomer distance vector and the TDMs is $\theta = 11^\circ$.

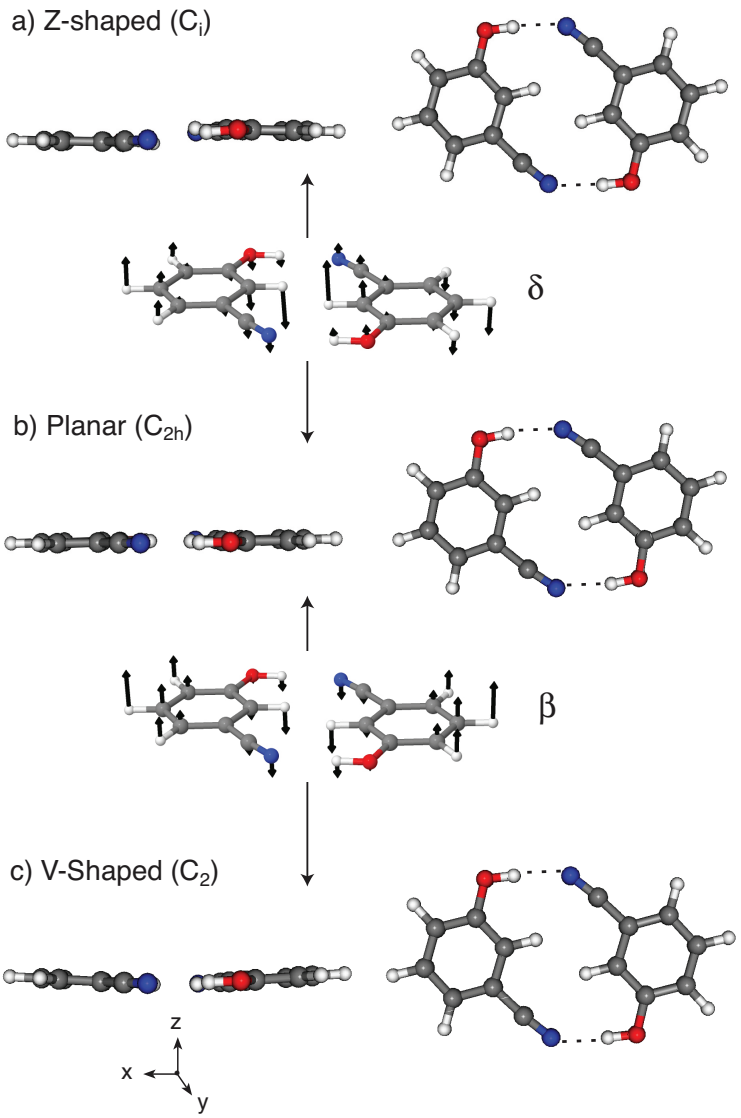

Figure 2: SCS-CC2/aug-cc-pVTZ optimized isomers of (*meta*-cyanophenol)$_2$. Left: side views, right: top views. The intermolecular vibrations δ and β interconvert the C_i, C_{2h} and C_2 structures.

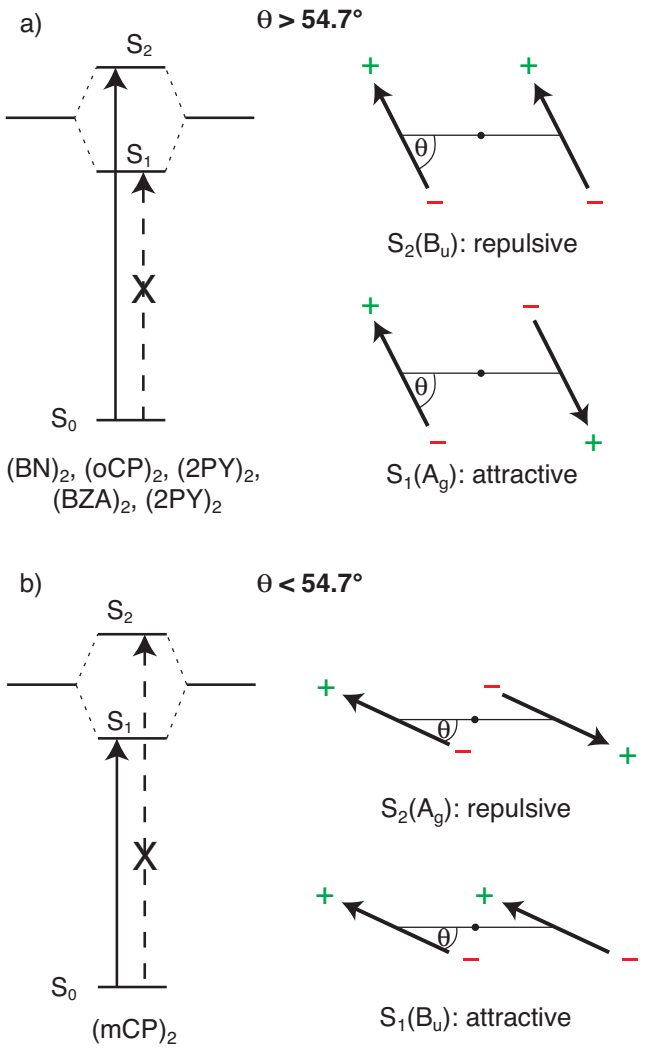

Figure 3: Electric-dipole allowed and forbidden $S_0 \rightarrow S_1/S_2$ transitions (left) and corresponding transition dipole-moment vector directions in excitonic homodimers. (a) For $\theta > 54.7°$, (b) for $\theta < 54.7°$. Full and dashed vertical arrows symbolize allowed and forbidden electronic transitions. Examples of spectroscopically investigated homodimers are given for both cases, see the text.

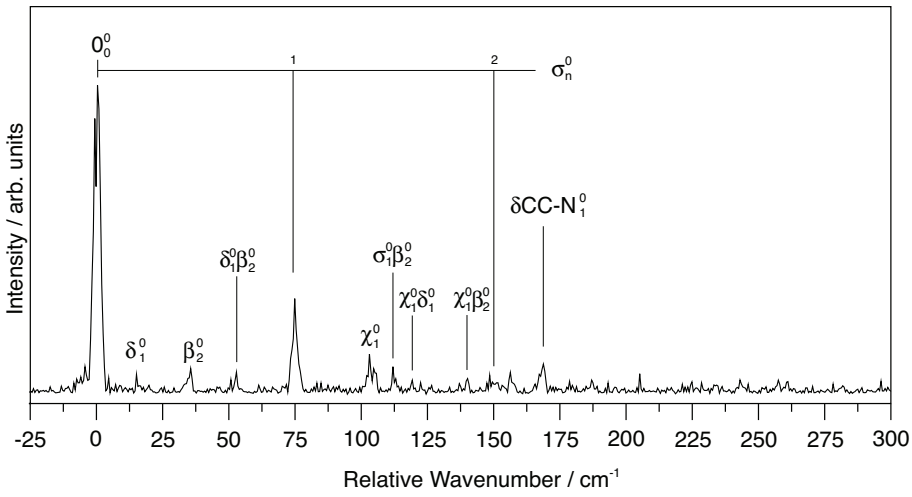

Figure 4: Dispersed fluorescence spectrum of (*m*-cyanophenol)$_2$ with band assignments. The wavenumber scale is relative to the 0_0^0 band at 33255 cm^{-1}.

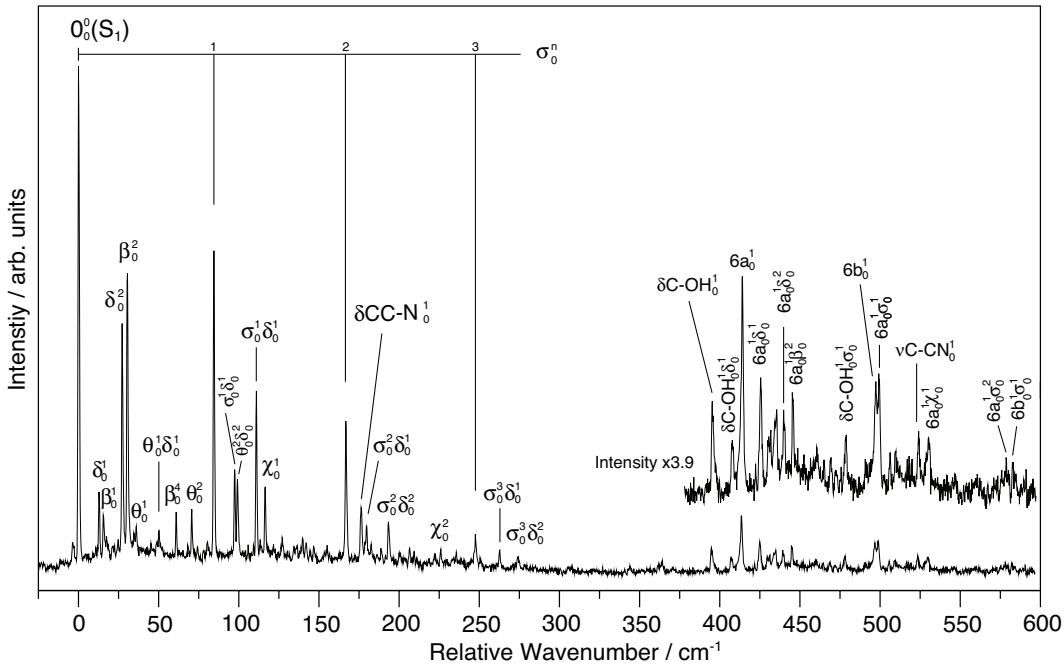

Figure 5: Two-color resonant two-photon ionization spectrum of (*meta*-cyanophenol)$_2$ with assigned vibronic transitions. The scale is relative to the 0_0^0 band at 33255 cm^{-1}.

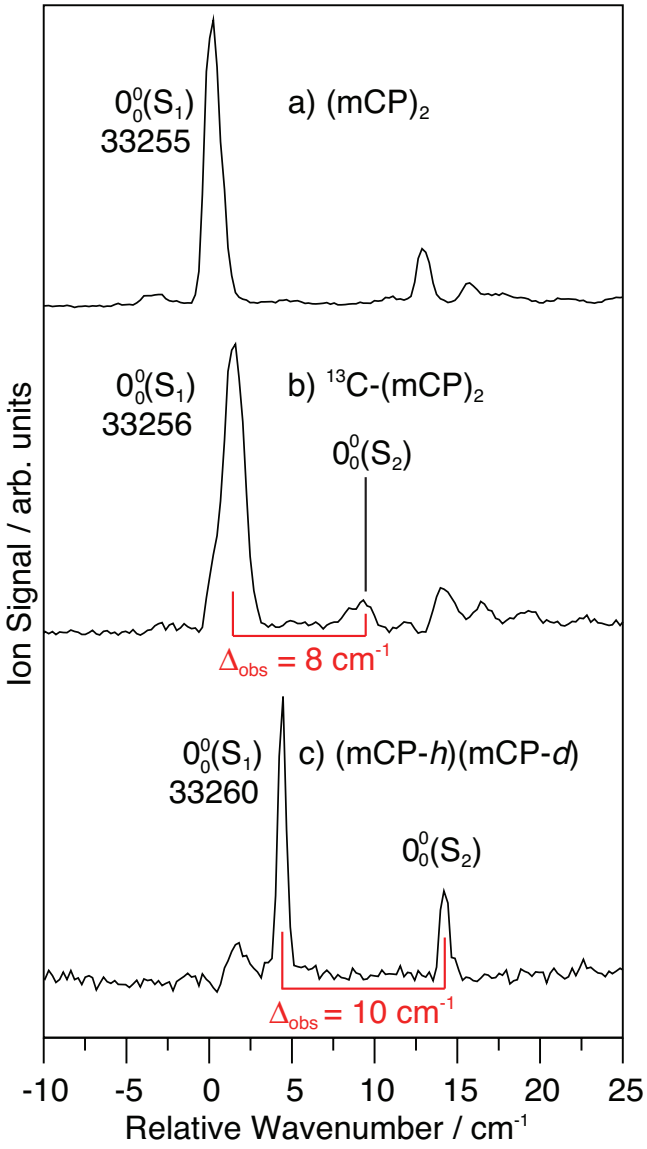

Figure 6: 2C-R2PI spectra of (a) (*meta*-cyanophenol)$_2$, (b) ^{13}C-substituted and c) H/D substituted heterodimers in the 0_0^0 band region. The scale is relative to the 0_0^0 band of $(mCP)_2$ at 33255 cm^{-1}. The 0_0^0 band of ^{13}C-$(mCP)_2$ is at 33256 cm^{-1}, that of (mCP-*h*)(mCP-*d*) at 33260 cm^{-1}.

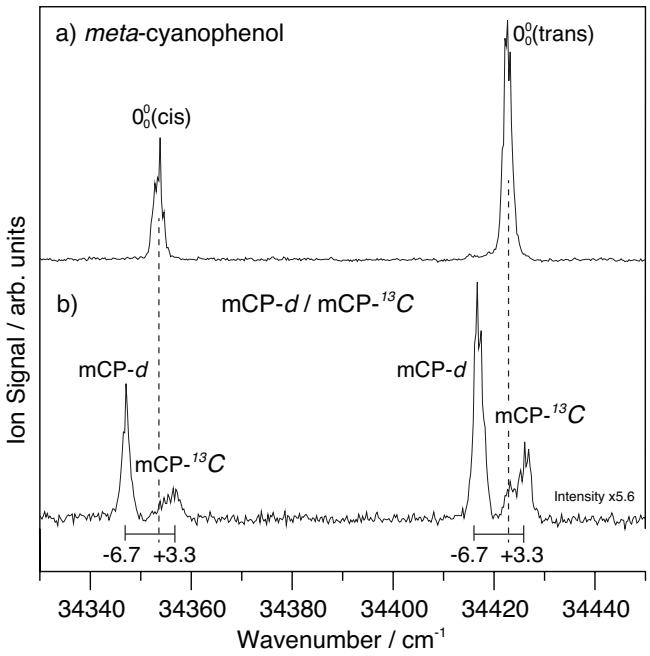

Figure 7: 2C-R2PI spectra of the 0_0^0 band region of cis- and trans-*meta*-cyanophenol. (a) mCP mass channel (m/e=119), b) mCP+1 mass channel (m/e=120) showing the signals of ^{13}C-mCP and mCP-*d*.

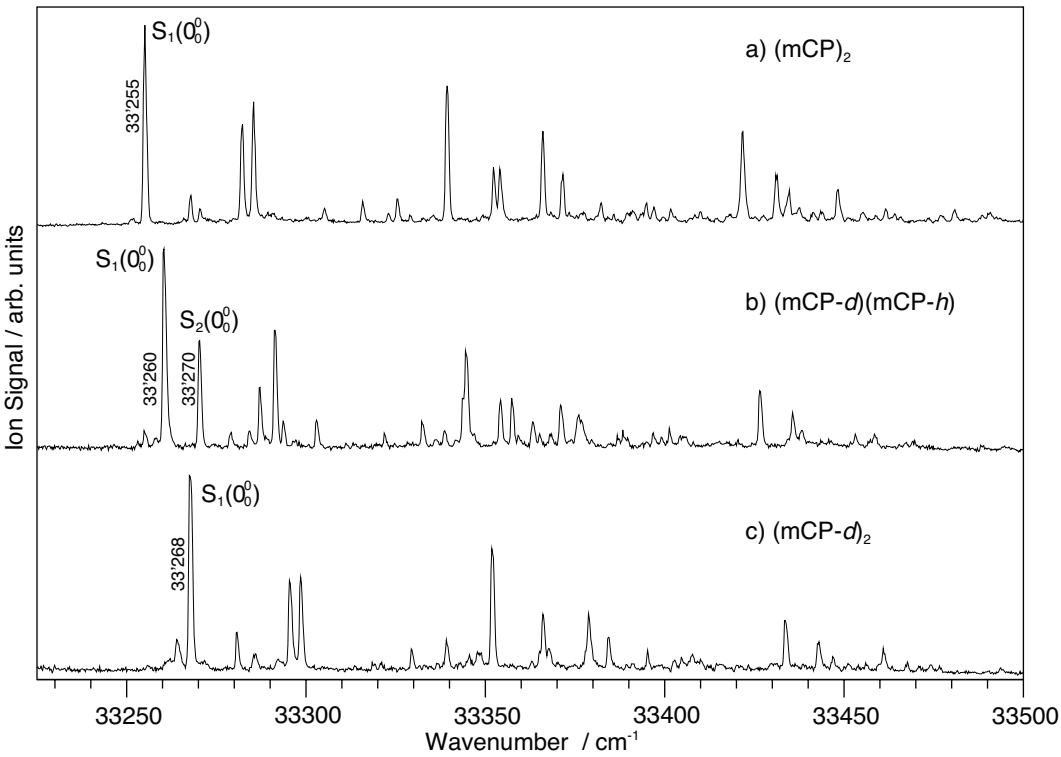

Figure 8: 2C-R2PI spectra of (a) all-*h*-(*m*-cyanophenol)$_2$, (b) (*m*-cyanophenol-*h*)(*m*-cyanophenol-*d*) and (c) (*m*-cyanophenol-*d*)$_2$.

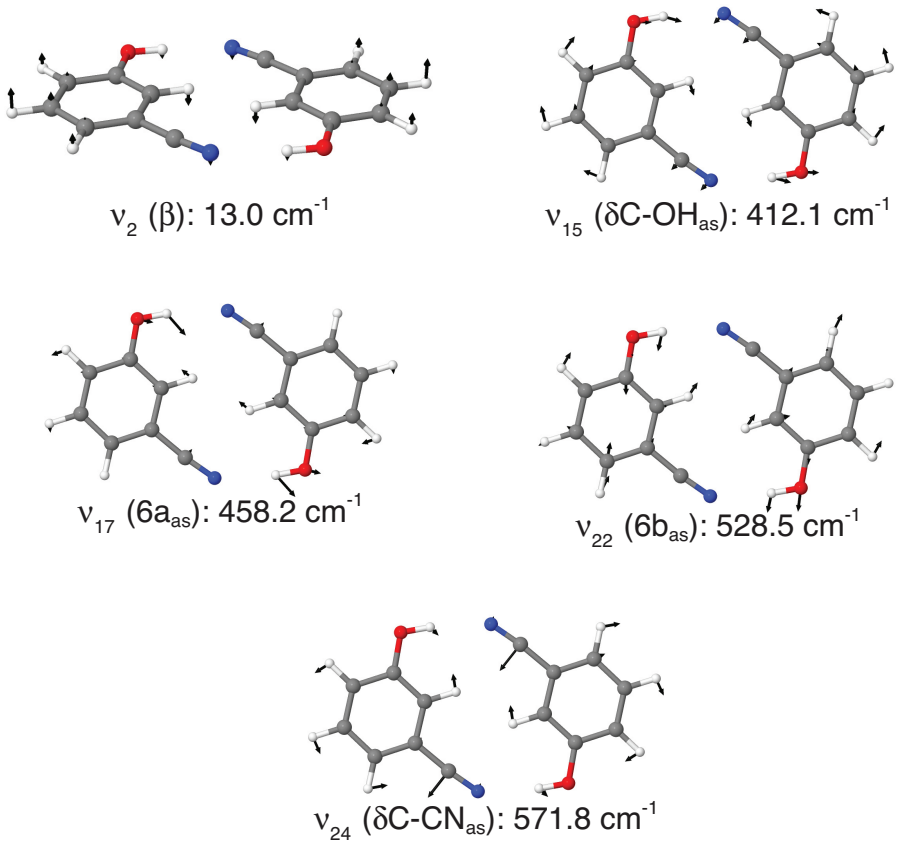

Figure 9: SCS-CC2/aVTZ calculated eigenvectors of the low-frequency antisymmetric (a_u) modes of (*m*-cyanophenol)$_2$.

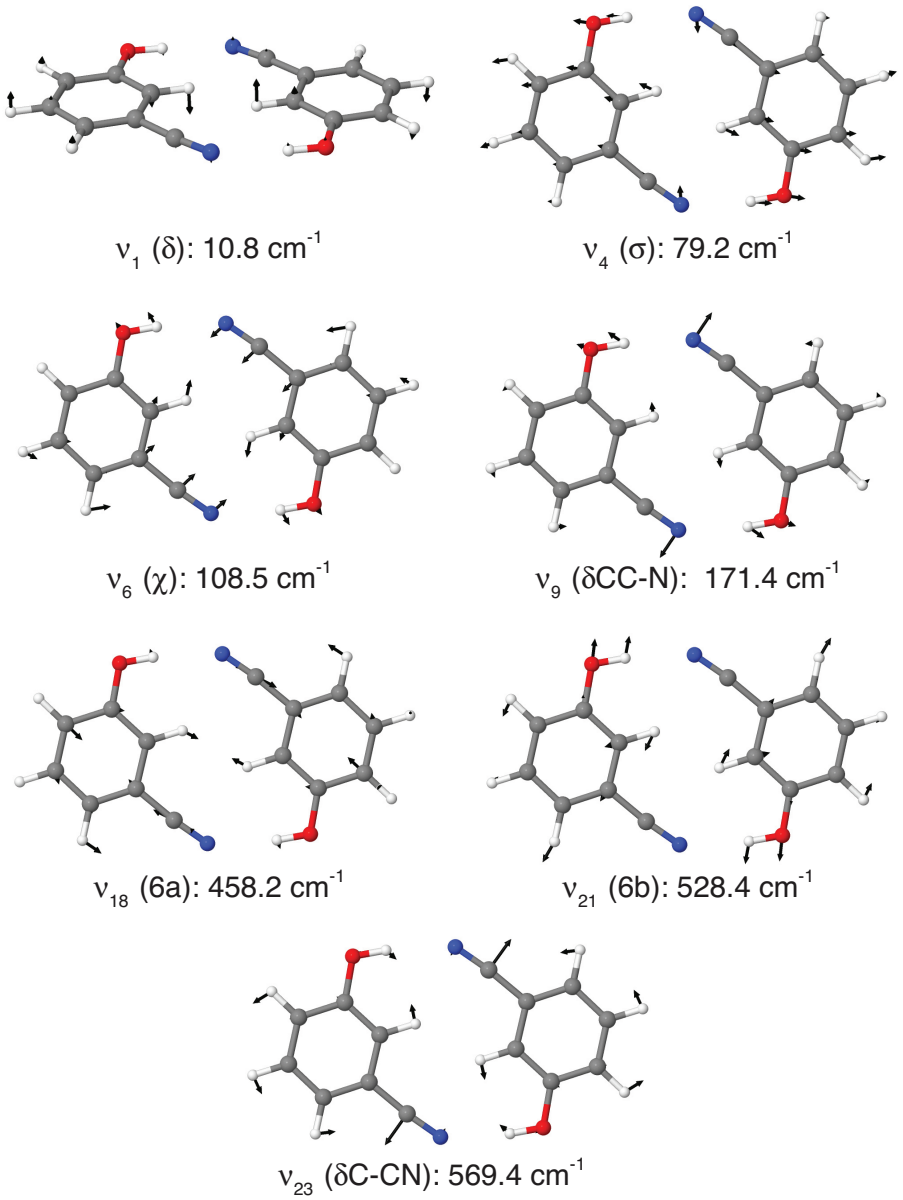

Figure 10: SCS-CC2/aVTZ calculated eigenvectors of the low-frequency totally-symmetric (a_g) modes of (*m*-cyanophenol)$_2$.

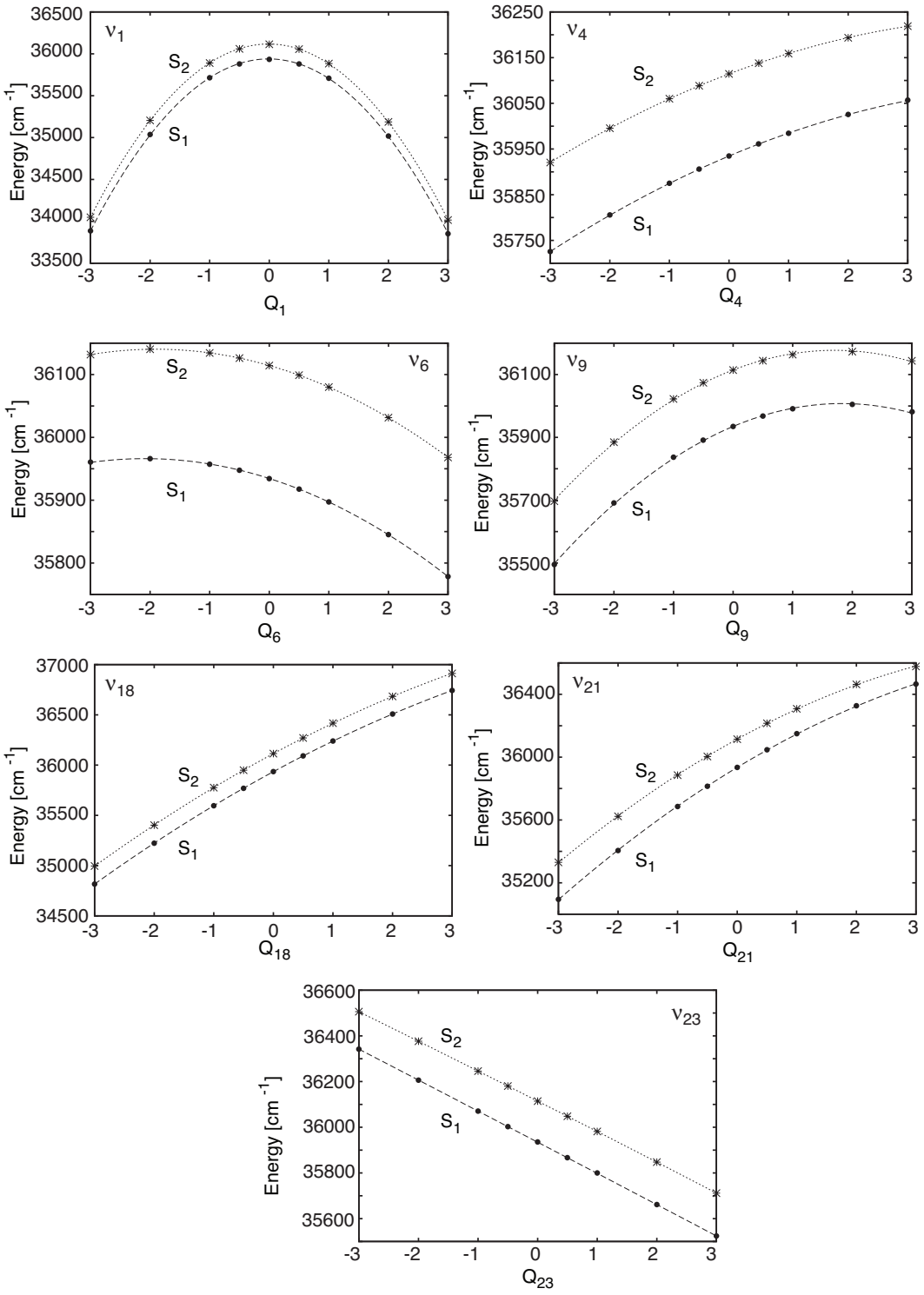

Figure 11: Least-squares fits to the calculated S_1 and S_2 excitation energies of (*m*-cyanophenol)$_2$ along the normal-modes Q_i of the modes ν_1, ν_4, ν_6, ν_9, ν_{18}, ν_{21} and ν_{23}. The corresponding vibrational eigenvectors are shown in Figs. 10 and fig:vibs-au. The *ab initio* energies are shown as dots for S_1 and crosses for S_2.

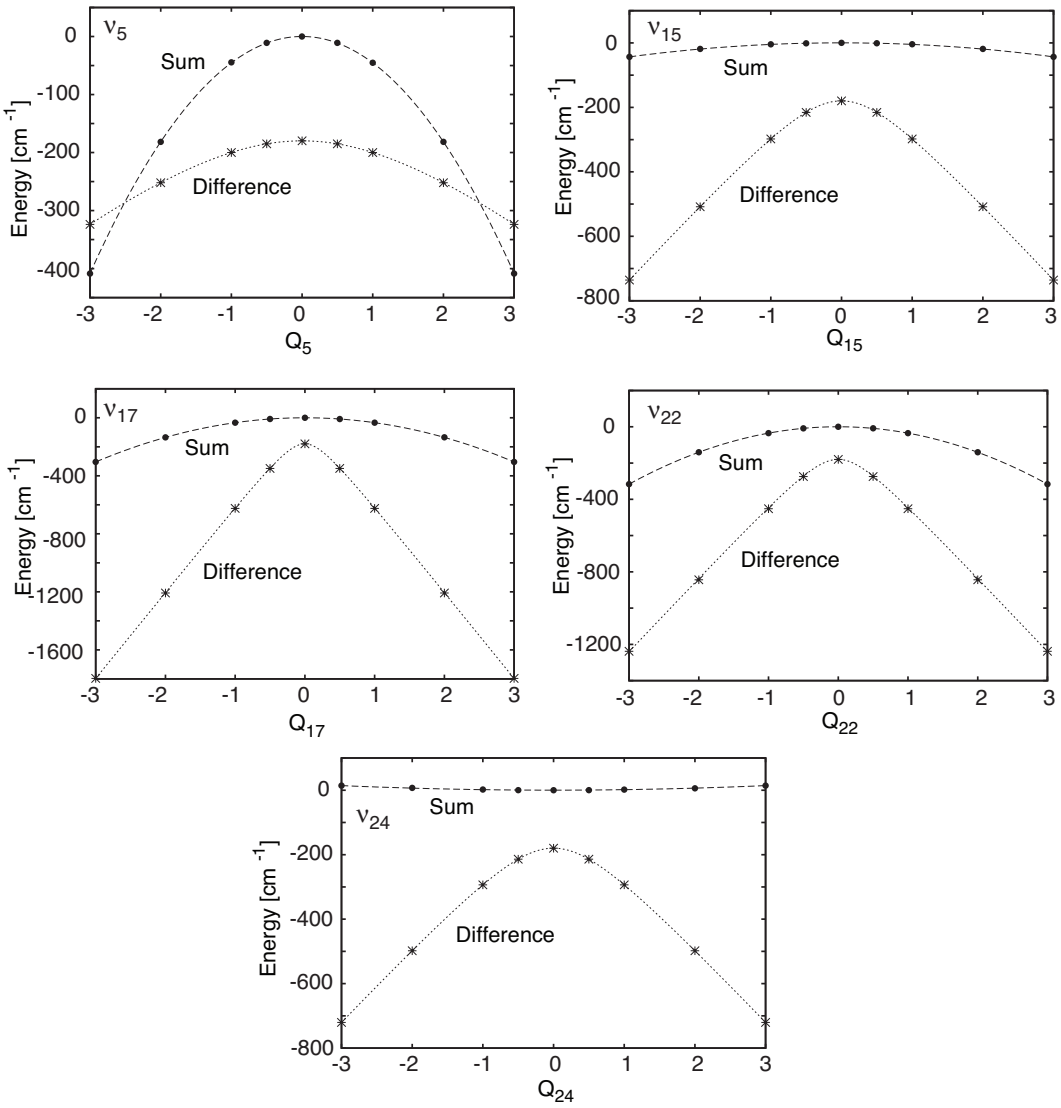

Figure 12: Least-squares fits to the sum (dashed) and difference (dotted) of the excitation energies along the normal-mode eigenvectors of the vibrations ν_5, ν_{15}, ν_{17} and ν_{24}. The *ab initio* energies are shown as dots for S_1 and crosses for S_2.

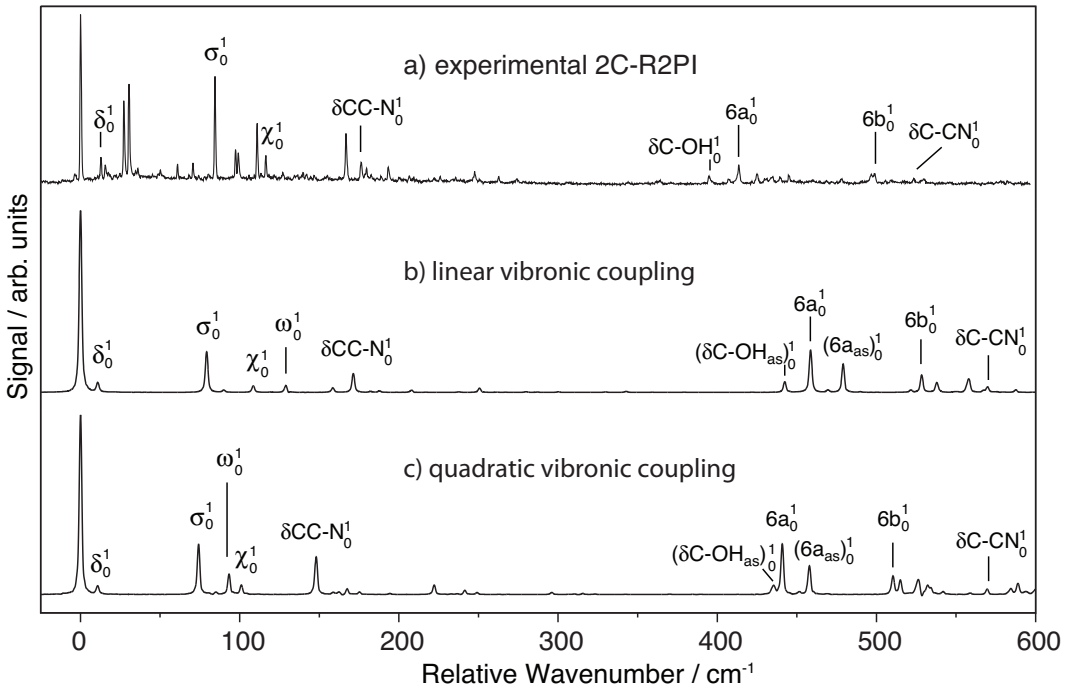

Figure 13: (a) Experimental 2C-R2PI spectrum of $(mCP)_2$ compared to the MCTDH simulated spectra based on (b) the LVC and (c) the QVC model.

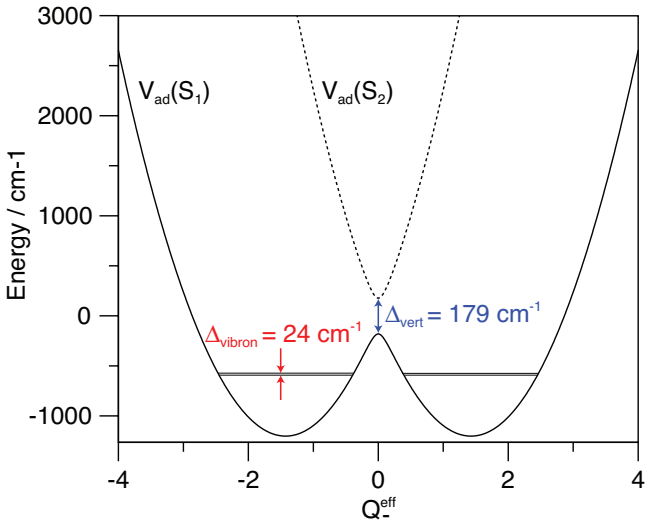

Figure 14: S_1 and S_2 excited-state adiabatic potential energy surfaces along the effective mode Q_{-}^{eff}. The vertical excitation energy splitting Δ_{vert} at the ground state equilibrium geometry $Q_{-}^{eff} = 0$ is identical to the calculated Davydov splitting Δ_{el}.

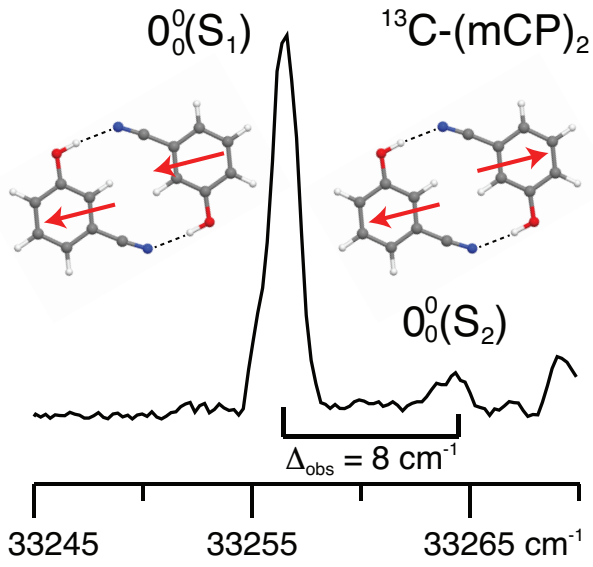

Figure 15: TOC graphic